

1 **Source-Resolved Volatility and Oxidation State Decoupling in**  
2 **Wintertime Organic Aerosols in Seoul**

3  
4 Hwajin Kim<sup>1,2,\*</sup>, Jiwoo Jeong<sup>1</sup>, Jihye Moon<sup>1</sup>, Hyun Gu Kang<sup>2,3</sup>

5 <sup>1</sup>Department of Environmental Health Sciences, Graduate School of Public Health, Seoul National University, 08826 Seoul,  
6 South Korea

7 <sup>2</sup>Institute of Health and Environment, Graduate School of Public Health, Seoul National University, 08826 Seoul, South Korea

8 <sup>3</sup>Now at Multiphase Chemistry Department, Max Planck Institute for Chemistry, 55128 Mainz, Germany

9 *Correspondence to:* Hwajin Kim (khj0116@snu.ac.kr)

10 **Abstract.**

11 Organic aerosols (OA) are key components of wintertime urban haze, but the relationship between their oxidation  
12 state and volatility—critical for understanding aerosol evolution and improving model predictions—remains poorly  
13 constrained. While oxidation–volatility decoupling has been observed in laboratory studies, field-based evidence  
14 under real-world conditions is scarce, particularly during severe haze episodes. This study presents a field-based  
15 investigation of OA sources and their volatility characteristics in Seoul during a winter haze period, using a  
16 thermodenuder coupled with a high-resolution time-of-flight aerosol mass spectrometer (HR-ToF-AMS).

17 Positive matrix factorization resolved six OA factors: hydrocarbon-like OA, cooking, biomass burning, nitrogen-  
18 containing OA (NOA), less-oxidized oxygenated OA (LO-OOA), and more-oxidized OOA (MO-OOA). Despite  
19 having the highest oxygen-to-carbon ratio (~1.15), MO-OOA exhibited unexpectedly high volatility, indicating a  
20 decoupling between oxidation state and volatility. We attribute this to fragmentation-driven aging and autoxidation  
21 under stagnant conditions with limited OH exposure. In contrast, LO-OOA showed lower volatility and more  
22 typical oxidative behavior.

23 Additionally, NOA—a rarely resolved factor in wintertime field studies—was prominent during cold, humid, and  
24 stagnant conditions and exhibited chemical and volatility features similar to biomass burning OA, suggesting a  
25 shared combustion origin and meteorological sensitivity.

26 These findings provide one of the few field-based demonstrations of oxidation–volatility decoupling in ambient  
27 OA and highlight how source-specific properties and meteorology influence OA evolution. The results underscore  
28 the need to refine OA representation in chemical transport models, especially under haze conditions.

29 **Keywords:** Organic aerosol volatility, HR-ToF-AMS, Thermodenuder, elemental ratios, aging, fragmentation

30 **1 Introduction**

31 Atmospheric aerosols affect both human health and the environment by reducing visibility (Ghim et al., 2005; Zhao  
32 et al., 2013) and contributing to cardiovascular and respiratory diseases (Hamanaka et al., 2018; Manalisidis et al.,  
33 2020). In addition, aerosols play a significant role in climate change by scattering or absorbing solar radiation and  
34 modifying cloud properties (IPCC AR6). Among the various aerosol components—including sulfate, nitrate,  
35 ammonium, chloride, crustal materials, and water—organic aerosols (OA) are particularly important to characterize,  
36 as they account for 20–90% of submicron particulate matter (Zhang et al., 2007). Identifying OA sources and  
37 understanding their behavior are critical for effective air quality management; however, this is particularly  
38 challenging due to the vast diversity and dynamic nature of OA compounds, which originate from both natural and  
39 anthropogenic sources. Unlike inorganic aerosols, organic aerosols (OAs) evolve continuously through complex  
40 atmospheric reactions, influenced by emission sources, meteorological conditions, and aerosol properties (Jimenez  
41 et al., 2009; Hallquist et al., 2009; Robinson et al., 2007; Donahue et al., 2006; Ng et al., 2010; Cappa and Jimenez,  
42 2010).

43 Volatility is a key parameter for characterizing organic aerosol (OA) properties, as it governs gas-to-particle  
44 partitioning behavior and directly influences particle formation yields (Sinha et al., 2023). The classification of OA  
45 species based on their volatility—from extremely low-volatility (ELVOC) to semi-volatile (SVOC) and  
46 intermediate-volatility (IVOC) compounds—is central to the conceptual framework of secondary OA (SOA)  
47 formation and growth (Donahue et al., 2006). It also affects atmospheric lifetimes and human exposure by  
48 determining how long aerosols remain suspended in the atmosphere (Glasius and Goldstein, 2016). Therefore,  
49 accurately capturing OA volatility is essential for improving predictions of OA concentrations and their  
50 environmental and health impacts. However, chemical transport models often significantly underestimate OA mass  
51 compared to observations (Matsui et al., 2009; Jiang et al., 2012; Li et al., 2017), largely due to incomplete  
52 precursor inventories and simplified treatment of processes affecting OA volatility. For instance, aging—through  
53 oxidation reactions such as functionalization and fragmentation—can significantly alter volatility by changing OA  
54 chemical structure (Robinson et al., 2007; Zhao et al., 2016). Early volatility studies primarily utilized thermal  
55 denuders (TD) coupled with various detection instruments to investigate the thermal properties of bulk OA  
56 (Huffman et al., 2008). The subsequent coupling of TD with the Aerosol Mass Spectrometer allowed for  
57 component-resolved volatility measurements, providing critical, quantitative insight into the properties of OA  
58 factors (e.g., SV-OOA vs. LV-OOA) across different regions (Paciga et al., 2016; Cappa and Jimenez, 2010). These  
59 component-resolved volatility data are often used to constrain the Volatility Basis Set (VBS)—the current state-of-

60 the-art framework for modeling OA partitioning and evolution (Donahue et al., 2006). However, a limitation in  
61 many field studies is that the TD-AMS thermogram data are rarely translated into quantitative VBS distributions  
62 for individual OA factors, which limits their direct use in chemical transport models. Furthermore, the volatility of  
63 OOA during extreme haze conditions, where the expected inverse correlation between oxidation (O:C) and  
64 volatility can break down (Jimenez et al., 2009), remains poorly characterized, particularly in East Asia's highly  
65 polluted winter environments. A recent study in Korea further highlighted the importance of accounting for such  
66 processes when interpreting OA volatility under ambient conditions (Kang et al., 2022). Given its central role in  
67 OA formation, reaction, and atmospheric persistence, volatility analysis is critical for bridging the gap between  
68 measurements and model performance.

69 Traditionally, due to the complexity and variability of OA, the oxygen-to-carbon (O:C) ratio has been used as a  
70 proxy for estimating volatility. In general, higher O:C values indicate greater oxidation and lower volatility  
71 (Jimenez et al., 2009). Accordingly, many field studies classify oxygenated OA (OOA) into semi-volatile OOA  
72 (SV-OOA) and low-volatility OOA (LV-OOA) based on their O:C ratios (Ng et al., 2010; Huang et al., 2010; Mohr  
73 et al., 2012). However, this relationship is not always straightforward. Fragmentation during oxidation can increase  
74 both O:C and volatility simultaneously, disrupting the expected inverse correlation (Jimenez et al., 2009). In  
75 laboratory experiments, yields of highly oxidized SOA have been observed to decrease due to fragmentation (Xu  
76 et al., 2014; Grieshop et al., 2009). These findings suggest that while O:C can offer useful insights, it is insufficient  
77 alone to represent OA volatility. Direct volatility measurements, especially when paired with chemical composition  
78 data, are necessary to improve our understanding of OA sources and aging processes.

79 In this study, we investigate the sources and volatility characteristics of OA in Seoul during winter. Wintertime OA  
80 presents additional challenges due to its high complexity. During winter, emissions from combustion sources such  
81 as biomass burning and residential heating significantly increase, contributing large amounts of primary OA (Kim  
82 et al., 2017). Meanwhile, low ambient temperatures and reduced photochemical activity affect the formation and  
83 evolution of secondary OA (SOA). Frequent haze events further complicate the aerosol properties by extending  
84 aging times and increasing particle loadings. These overlapping sources and atmospheric conditions make winter  
85 OA particularly difficult to characterize and predict. Despite Seoul's significance for air quality management,  
86 comprehensive studies on OA volatility during winter remain limited. To address these goals, we conducted real-  
87 time, high-resolution measurements using a high-resolution time-of-flight aerosol mass spectrometer (HR-ToF-  
88 AMS) coupled with a thermodenuder (TD). The objectives of this study are to: (1) improve the understanding of

89 wintertime OA in Seoul, (2) characterize the volatility of OA associated with different sources, and (3) explore the  
90 relationship between OA volatility and chemical composition.

91 **2 Experimental methods**

92 **2.1 Sampling Site and Measurement Period**

93 We conducted continuous real-time measurements in Seoul, South Korea, from 28 November to 28 December 2019.  
94 The sampling site was located in the northeastern part of the city ( $37.60^{\circ}$  N,  $127.05^{\circ}$  E), approximately 7 km from  
95 the city center, surrounded by major roadways and mixed commercial–residential land use. Air samples were  
96 collected at an elevation of approximately 60 meters above sea level, on the fifth floor of a building. A detailed site  
97 description has been reported previously for winter Seoul (Kim et al., 2017). During this period, the average  
98 ambient temperature was  $1.76 \pm 4.3^{\circ}$  C, and the average relative humidity (RH) was  $56.9 \pm 17.5\%$ , based on data  
99 from the Korea Meteorological Administration (<http://www.kma.go.kr>).

100 **2.2 Instrumentation and Measurements**

101 The physico-chemical properties of non-refractory  $PM_1$  (NR- $PM_1$ ) species—including sulfate, nitrate, ammonium,  
102 chloride, and organics—were measured using an Aerodyne high-resolution time-of-flight aerosol mass  
103 spectrometer (HR-ToF-AMS) (DeCarlo et al., 2006).  $PM_1$  mass in this study is taken as NR- $PM_1$  (from AMS) +  
104 black carbon (BC; measured by MAAP), which is appropriate for winter Seoul where refractory  $PM_1$  (metal/sea-  
105 salt/crustal) is minor and dust events were excluded (e.g., Kim et al., 2017; Nault et al., 2018; Kang et al., 2022;  
106 Jeon et al., 2023). Data were acquired at 2.5-minute intervals, alternating between V and W modes. The V mode  
107 provides higher sensitivity but lower resolution, suitable for mass quantification, whereas the W mode offers higher  
108 mass resolution but lower sensitivity, used here for OA source apportionment. Simultaneously, black carbon (BC)  
109 concentrations were measured at 1-minute intervals using a multi-angle absorption photometer (MAAP; Thermo  
110 Fisher Scientific, Waltham, MA, USA). Total  $PM_1$  mass was calculated as the sum of NR- $PM_1$  and BC.

111 Hourly trace gas concentrations (CO, O<sub>3</sub>, NO<sub>2</sub>, SO<sub>2</sub>) were obtained from the Gireum air quality monitoring station  
112 ( $37.61^{\circ}$  N,  $127.03^{\circ}$  E), managed by the Seoul Research Institute of Public Health and Environment. Meteorological

113 data (temperature, RH, wind speed/direction) were collected from the nearby Jungreung site (37.61° N, 127.00° E).  
114 All data are reported in Korea Standard Time (UTC+9).

115 To examine aerosol volatility, a thermodenuder (TD; Envalytix LLC) was installed upstream of the HR-ToF-AMS.  
116 Details are provided in Supplementary Section S1 Kang et al. (2022). Briefly, ambient flow alternated every 5  
117 minutes between a TD line and a bypass line at  $1.1 \text{ L min}^{-1}$ . Residence time in the TD line was  $\sim 6.3 \text{ s}$ . The TD  
118 setup included a 50 cm heating section followed by an adsorption unit. Heated particles were stripped of volatile  
119 species, while the downstream carbon-packed section prevented recondensation. TD temperature cycled through  
120 12 steps (30 to 200 °C), with each step lasting 10 min (total cycle = 120 min). AMS V and W modes were alternated  
121 during the same cycle. The heater was pre-adjusted to the next temperature while the bypass was active.

122

123 **2.3 Data Analysis**

124

125 **2.3.1 Data analysis and OA Source Apportionment**

126 HR-AMS data were processed using SQUIRREL v1.65B and PIKA v1.25B. Mass concentrations of non-refractory  
127 PM<sub>1</sub> (NR-PM<sub>1</sub>) species were derived from V-mode data, while high-resolution mass spectra (HRMS) and the  
128 elemental composition of organic aerosols (OA) were obtained from W-mode data. NR-PM<sub>1</sub> quantification  
129 followed established AMS protocols (Ulbrich et al., 2009; Zhang et al., 2011). Both the bypass and TD streams  
130 were processed using a time-resolved, composition-dependent collection efficiency CE(t) following Middlebrook  
131 et al. (2012). TD heating can modify particle water and phase state/mixing and thereby influence CE beyond  
132 composition (Huffman et al., 2009), but prior TD-AMS studies indicate that such effects are modest and largely  
133 multiplicative, which do not distort thermogram shapes or T<sub>50</sub> ordering (Faulhaber et al., 2009; Cappa & Jimenez,  
134 2010). In our data, the CE(t) statistics for the two lines were similar (campaign-average CE: TD =  $0.55 \pm 0.08$ ;  
135 bypass =  $0.53 \pm 0.04$ ;  $\Delta = 0.02 \approx 3.7\%$ , below the combined uncertainty  $\approx 0.09$ ). We therefore report volatility  
136 metrics with these line-specific CE(t) corrections applied and interpret potential residual CE effects as minor. For  
137 organics, elemental ratios (O:C, H:C, and OM/OC) were calculated using the Improved-Ambient (IA) method  
138 (Canagaratna et al., 2015). Positive Matrix Factorization (PMF) was applied to the HRMS of organics using the  
139 PMF2 algorithm (v4.2, robust mode) (Paatero and Tapper, 1994). The HRMS and corresponding error matrices  
140 from PIKA were analyzed using the PMF Evaluation Tool v2.05 (Ulbrich et al., 2009). Data pretreatment followed  
141 established protocols (Ulbrich et al., 2009; Zhang et al., 2011).

142 A six-factor solution (fPeak = 0; Q/Q\_expected = 3.56) was selected as optimal (Fig. S1). The resolved OA sources  
143 included hydrocarbon-like OA (HOA; 14%; O:C = 0.13), cooking-related OA (COA; 21%; O:C = 0.18), nitrogen-  
144 enriched OA (NOA; 2%; O:C = 0.22), biomass-burning OA (BBOA; 13%; O:C = 0.25), less-oxidized oxygenated  
145 OA (LO-OOA; 30%; O:C = 0.68), and more-oxidized oxygenated OA (MO-OOA; 20%; O:C = 1.15) (Figs. S2 and  
146 S3). Alternative five- and seven-factor solutions were also evaluated. In the five-factor solution, the biomass  
147 burning source was not clearly resolved and appeared to be distributed across multiple factors. In the seven-factor  
148 solution, BBOA was further split into two separate factors without clear distinction or added interpretive value,  
149 making the six-factor solution the most physically meaningful and interpretable (Figs. S4 and S5). [To ensure the](#)  
150 [statistical robustness of this solution, we calculated uncertainties for each PMF factor using the bootstrap method](#)  
151 [\(100 iterations\) with the PET toolkit \(v2.05\) \(EPA, 2014; Xu et al., 2018; Srivastava et al., 2021\) \(Table S2 and](#)  
152 [Fig. S13\).](#)

153

### 154 2.3.2 Thermogram and Volatility Estimation

155 The chemical composition dependent mass fraction remaining (MFR) was derived at each TD temperature by  
156 dividing the corrected mass concentration of the TD line [p] by the average of the adjacent bypass lines [p-1] and  
157 [p+1]. Thermograms were corrected for particle loss, estimated using reference substances like NaCl, which exhibit  
158 minimal evaporation (Huffman et al., 2009; Saha et al., 2014; Kang et al., 2022). OA factor concentrations at each  
159 TD temperature were derived via multivariate linear regression between post-TD HRMS and ambient OA factor  
160 HRMS profiles as described in Zhou et al., 2017.

161 Volatility distributions were modeled using the thermodenuder mass transfer model from Riipinen et al. (2010) and  
162 Karnezi et al. (2014), implemented in Igor Pro 9 (Kang et al., 2022). OA mass was distributed into eight logarithmic  
163 saturation concentration bins ( $C^*$ : 1000 to  $0.0001 \mu\text{g m}^{-3}$ ). Modeled MFRs were fit to observations using Igor's  
164 "FuncFit" function, repeated 1,000 times per OA factor to determine best-fit results. The model assumes no thermal  
165 decomposition and includes adjustable parameters: mass accommodation coefficient ( $\alpha_m$ ) and enthalpy of  
166 vaporization ( $\Delta H_{\text{exp}}$ ), randomly sampled within literature-based ranges (Table S1).

167

## 168 3 Results and discussion

169 **3.1 Overview of PM<sub>1</sub> Composition and OA Sources**

170 We conducted continuous measurements from 28 November to 28 December 2019, characterizing a winter period  
171 with a mean PM<sub>1</sub> concentration of  $27.8 \pm 15.3 \mu\text{gm}^{-3}$ . This concentration is characterized as moderate; it closely  
172 matches historical winter PM<sub>1</sub> means in Seoul (Kim et al., 2017) and implies an equivalent PM<sub>2.5</sub> concentration is  
173 about  $34.8 \mu\text{gm}^{-3}$  (using a Korea-specific PM<sub>1</sub>/PM<sub>2.5</sub>  $\approx 0.8$  (Kwon et al., 2023), which is near the national 24-h PM<sub>2.5</sub>  
174 standard ( $35 \mu\text{gm}^{-3}$ ) (AirKorea). The full co-evolution of PM<sub>1</sub>, gaseous pollutants, and meteorological conditions  
175 is provided in Fig. S6, showing an average ambient temperature of  $1.76 \pm 4.3^\circ\text{C}$  and average relative humidity (RH)  
176 of  $56.9 \pm 17.5\%$  during the study.

177 Figure 1 summarizes the overall non-refractory submicron aerosol (NR-PM<sub>1</sub>) composition and the identified OA  
178 factors. Organics (41%) and nitrate (30%) were the most abundant chemical components of PM<sub>1</sub>, followed by  
179 ammonium (12%), sulfate (10%), BC (5%), and chloride (3%) (Fig. 1a). Among the organic aerosols, six OA  
180 factors were identified during the winter of 2019: hydrocarbon-like OA (HOA; 14%; O:C = 0.13), cooking-related  
181 OA (COA; 21%; O:C = 0.18), nitrogen-enriched OA (NOA; 2%; O:C = 0.22), biomass burning OA (BBOA; 13%;  
182 O:C = 0.25), and two types of secondary organic aerosols—less-oxidized oxygenated OA (LO-OOA; 30%; O:C =  
183 0.68) and more-oxidized oxygenated OA (MO-OOA; 20%; O:C = 1.15) (Fig. 1e and Fig. S2). These compositions  
184 are consistent with previous wintertime observations in Kim et al. (2017), with the exception of [newly resolved](#)  
185 [NOA source. In the following sections, we describe each OA factor in the order of secondary OA \(SOA\), primary](#)  
186 [OA \(POA\) and , and finally introduce NOA, which—while related to combustion POA—emerged as a distinct,](#)  
187 [nitrogen-rich factor under the winter conditions of this study.](#)

188 PM<sub>1</sub> mass concentrations varied widely, ranging from  $4.61$  to  $91.4 \mu\text{g m}^{-3}$ , largely due to two severe haze episodes  
189 that occurred between December 7–12 and December 22–26 (Fig. 1). During these episodes, average  
190 concentrations increased significantly, driven primarily by elevated levels of nitrate and organic aerosols—  
191 particularly MO-OOA and NOA (Fig. 1f,g). Back-trajectory clustering shows frequent short-range recirculation  
192 over the Seoul Metropolitan Area during haze (Cluster 1; Fig. S8), and the time series indicates persistently low  
193 surface wind speeds during these periods ( $1.73 \pm 0.89$  vs.  $2.34 \pm 1.18$  (clean)) (Fig. S6). [These patterns indicate](#)  
194 [stagnation-driven accumulation of local emissions, consistent with the simultaneous increase of MO-OOA and](#)  
195 [NOA that are examined in detail in subsequent sections. together pointing to stagnation driven accumulation of](#)  
196 [local emissions; the concurrent increases in MO-OOA and NOA are therefore consistent with enhanced in-city](#)

197 formation under stagnant conditions. Such haze episodes, characterized by local emission buildup and secondary  
198 aerosol production, are a typical wintertime feature, as also reported in Kim et al. (2017).

199 **3.1.21 Secondary organic aerosols (SOA)**

200 In this study, two OOA factors—more-oxidized OOA (MO-OOA) and less-oxidized OOA (LO-OOA)—were  
201 identified, together accounting for approximately half of the total organic aerosol (OA) mass. This fraction is  
202 notably higher than that reported in previous wintertime urban studies (Kim et al., 2017; Zhang et al., 2007).  
203 Both OOAAs exhibited characteristic mass spectral features, including prominent peaks at  $m/z$  44 ( $\text{CO}_2^+$ ) and  $m/z$   
204 43 ( $\text{C}_2\text{H}_3\text{O}^+$ ), which are widely recognized as markers of oxygenated organics (Fig. S2e, S3f). The oxygen-to-  
205 carbon (O:C) ratios for MO-OOA and LO-OOA were 1.15 and 0.68, respectively, indicating both factors are  
206 highly oxidized relative to the primary OA factors (HOA, COA, BBOA) and that MO-OOA is substantially more  
207 oxidized than LO-OOA. The O:C ratio of MO-OOA was especially  
208 elevated, exceeding those reported in previous Seoul campaigns—0.68 in winter 2015 (Kim et al., 2017), 0.99  
209 in spring 2019 (Kim et al., 2020), and 0.78 in fall 2019 (Jeon et al., 2023)—while the LO-OOA ratio was within  
210 a similar range.

211

212 MO-OOA showed strong correlations with secondary inorganic species such as nitrate ( $r = 0.90$ ), ammonium ( $r =$   
213 0.92), and sulfate ( $r = 0.81$ ), consistent with its formation through regional and local photochemical aging processes  
214 (Fig. S3). In contrast, LO-OOA exhibited only modest correlations with sulfate, nitrate, and ammonium ( $r = 0.50$ ,  
215 0.51, and 0.42, respectively). This weaker coupling indicates that LO-OOA represents a less aged oxygenated OA  
216 component (fresh SOA), distinguishable from the more aged, highly processed MO-OOA which tracks closely with  
217 secondary inorganic species. Regarding potential primary influence, LO-OOA does not exhibit a pronounced  $m/z$   
218 60 (levoglucosan) signal (Figs. S2 and 9). While the levoglucosan marker ( $f_{60}$ ) is known to diminish with  
219 atmospheric aging and can become weak or undetectable downwind (Hennigan et al., 2010; Cubison et al., 2011),  
220 the absence of a distinct peak combined with the separation from inorganic salts suggests that LO-OOA is best  
221 characterized as freshly formed secondary organic aerosol likely originating from the rapid oxidation of local  
222 anthropogenic precursors, rather than a primary emission source.

223 **MO-OOA showed strong correlations with secondary inorganic species such as nitrate ( $r = 0.90$ ),**  
224 **ammonium ( $r = 0.92$ ), and sulfate ( $r = 0.81$ ), consistent with its formation through regional and local**

225 photochemical aging processes (Fig. S3). In contrast, LO-OOA exhibited only modest correlations with  
226 sulfate, nitrate, and ammonium ( $r = 0.50, 0.51$ , and  $0.42$ , respectively), indicating that suggesting LO-OOA  
227 represents a less aged oxygenated OA component with possible influence from semi-primary precursors,  
228 rather than a factor strongly tied to secondary inorganic aerosol formation. additional contributions from  
229 semi-primary sources not closely linked to inorganic secondary formation (e.g., cooking, traffic, biomass  
230 burning). LO-OOA does not exhibit a pronounced  $m/z$  60 (levoglucosan) signal (Fig. S2); however, the  
231 levoglucosan marker ( $f_{60}$ ) is known to diminish with atmospheric aging and can become weak or  
232 undetectable downwind (Hennigan et al., 2010; Cubison et al., 2011). Taken together, the weaker coupling  
233 with secondary inorganics and the absence of a strong  $m/z$  60 peak indicate that LO-OOA is a mixture of  
234 aged secondary organics and aged semi-primary urban emissions, while a contribution from aged  
235 biomass burning influence cannot be ruled out..

236 3.1.3 Primary organic aerosols (POA)

237 **3.1.2 Primary organic aerosols (POA)**

238 Three primary organic aerosol (POA) factors were identified in this study: hydrocarbon-like OA (HOA), cooking-  
239 related OA (COA), and biomass burning OA (BBOA). These three components exhibited mass spectral and  
240 temporal characteristics consistent with previous observations in Seoul and other urban environments. HOA was  
241 characterized by dominant alkyl fragment ions ( $C_nH_{2n+1}^+$  and  $C_nH_{2n-1}^+$ ; Fig. S2a) and a low O:C ratio (0.13),  
242 consistent with traffic-related emissions (0.05–0.25) (Canagaratna et al., 2015). It showed strong correlations with  
243 vehicle-related ions  $C_3H_7^+$  ( $r = 0.79$ ) and  $C_4H_9^+$  ( $r = 0.86$ ) (Kim et al., 2017; Canagaratna et al., 2004; Zhang et al.,  
244 2005), and exhibited a distinct morning rush hour peak (06:00–08:00), followed by a decrease likely driven by  
245 boundary layer expansion (Fig. S3a).

246 COA, accounting for 21% of OA, showed higher contributions from oxygenated ions than HOA, with tracer peaks  
247 at  $m/z$  55, 84 and 98 (Fig. S2b) consistent with cooking emissions (Sun et al., 2011). COA showed an enhanced  
248 signal at  $m/z$  55 relative to  $m/z$  57, with a 55/57 ratio of 3.11, substantially larger than that of HOA (1.10). This  
249 elevated ratio is consistent with previously reported AMS COA spectra in urban environments (e.g., Allan et al.,  
250 2010; Mohr et al., 2012; Sun et al., 2011), supporting our factor assignment. It correlated strongly with cooking-

251 related ions such as  $\text{C}_3\text{H}_3\text{O}^+$  ( $r = 0.94$ ),  $\text{C}_5\text{H}_8\text{O}^+$  ( $r = 0.96$ ), and  $\text{C}_6\text{H}_{10}\text{O}^+$  ( $r = 0.98$ ) (Fig. S3h), and displayed  
252 prominent peaks during lunch and dinner hours, reflecting typical cooking activity patterns.

253 BBOA was identified based on characteristic ions at  $m/z$  60 ( $\text{C}_2\text{H}_4\text{O}_2^+$ ) and 73 ( $\text{C}_3\text{H}_5\text{O}^+$ ), both of which are  
254 associated with levoglucosan—a well-established tracer for biomass burning (Simoneit et al., 2002). Its relatively  
255 high  $f_{60}$  and low  $f_{44}$  values (Fig. S8a9) indicate that the BBOA observed in this study was relatively fresh and had  
256 not undergone extensive atmospheric aging (Cubison et al., 2011). Furthermore, BBOA exhibited moderate  
257 correlations with NOA in both diurnal profiles and time series (Fig. 2), particularly with nitrogen-containing ions  
258 such as  $\text{C}_2\text{H}_4\text{N}^+$  ( $r = 0.67$ ) and  $\text{C}_2\text{H}_6\text{N}^+$  ( $r = 0.56$ ) (Fig. 2 and S3), which are also dominant peaks in the NOA mass  
259 spectrum. This overlap suggests a potential shared emission source or co-emission scenario, consistent with the  
260 co-emission of both organic aerosols and reduced nitrogen-containing compounds. Regarding source location,  
261 several pathways can influence Seoul's biomass burning signature. First, urban/peri-urban small-scale burning (e.g.,  
262 solid-fuel use in select households, restaurant charcoal use, and intermittent waste burning) has been reported and  
263 can enhance BBOA locally (Kim et al., 2017). Second, nearby agricultural-residue burning in surrounding  
264 provinces occurs seasonally and can episodically impact the metropolitan area (Han et al., 2022). Third, regional  
265 transport from upwind regions (e.g., northeastern China/North Korea) can bring biomass burning influenced air  
266 masses under northerly/northwesterly flow (Lamb et al., 2018; Nault et al., 2018). In this dataset, the nighttime and  
267 early-morning enhancements, the BBOA–NOA co-variation, and trajectory clusters showing regional recirculation  
268 indicate a predominantly local/near-source contribution during the study period (Yoo et al., 2024), with episodic  
269 non-local influences remaining possible.

270 **3.1.13 Nitrogen-containing organic aerosol (NOA)**

271

272 A distinct nitrogen-containing organic aerosol (NOA) factor was resolved in this study, whereas earlier  
273 wintertime AMS–PMF analyses in Seoul did not isolate such a component. **Unlike previous wintertime aerosol**  
274 **studies in Seoul, this study successfully resolved a nitrogen-containing organic aerosol (NOA) factor by**  
275 **applying positive matrix factorization (PMF) to high-resolution AMS data. NOA contributed**  
276 **approximately 2% of the total organic aerosol (OA) mass comparable to urban observations in**

277 [Guangzhou \(3%; Chen et al., 2021\), Pasadena \(5%; Hayes et al., 2013\), and New York \(5.8%; Sun et al.,](#)  
278 [2011\).](#)

279 [Detection of particulate NOA using real time measurement has been challenging due to its low concentration](#)  
280 [and high volatility. Although Baek et al. \(2022\) identified nitrogen-containing species in Seoul via year-round](#)  
281 [filter-based molecular analysis, PMF based resolution of NOA in real time has not been previously reported.](#)  
282 [The successful identification in this study is likely attributable to favorable winter meteorological](#)  
283 [conditions specifically low temperatures \(-0.24 °C\) and persistently high relative humidity \(~57%\)](#)  
284 [compared to the 2017 winter season \(Kim et al., 2017\) that enhanced gas to particle partitioning of semi-](#)  
285 [volatile amines, thereby enabling their detection \(Fig. S2\). NOA concentrations frequently exceeded 1  \$\mu\text{g m}^{-3}\$](#)   
286 [when RH surpassed 60% \(Fig. 2\), supporting the importance of RH driven partitioning and the subsequent](#)  
287 [formation of low volatility aminium salts \(Rovelli et al., 2017\). Although extremely low temperatures may](#)  
288 [inhibit NOA formation due to the transition of aerosol particles into solid phase \(Ge et al., 2011; Srivastava](#)  
289 [et al., 2022\), the combination of consistently cold and humid conditions during the measurement period](#)  
290 [likely promoted the partitioning of semi-volatile amines into the particle phase.](#)

291 [In addition, episodic haze events further elevated NOA levels, increasing its contribution to OA from 1%](#)  
292 [during clean periods to as much as 3% \(Fig. 1f-h\). These high concentration events likely improved the](#)  
293 [signal-to-noise ratio, facilitating PMF resolution. Back trajectory analysis linked these events to regional](#)  
294 [recirculation patterns \(Cluster 1, Fig. S7\), suggesting a predominantly local origin consistent with the short](#)  
295 [atmospheric lifetimes and high reactivity of most amines \(Ge et al., 2011; Nielsen et al., 2012; Hanson et al.,](#)  
296 [2014\).](#)

297 The NOA factor exhibited the highest nitrogen-to-carbon (N:C) ratio (0.22) and the lowest oxygen-to-carbon (O:C)  
298 ratio (0.19) among all POA factors (Fig. S2), indicating a chemically reduced, nitrogen-rich composition. [The](#)  
299 [factor represents semi-volatile, reduced nitrogen species that originate from primary urban combustion sources but](#)  
300 [whose observed mass in the particle phase is enhanced by rapid secondary partitioning and salt formation \(Ge et](#)  
301 [al., 2011; You et al., 2014\).](#) The NOA mass spectrum was dominated by amine-related fragments including  $m/z$  30  
302 ( $\text{CH}_4\text{N}^+$ ), 44 ( $\text{C}_2\text{H}_6\text{N}^+$ ), 58 ( $\text{C}_3\text{H}_8\text{N}^+$ ), and 86 ( $\text{C}_5\text{H}_{12}\text{N}^+$ ) (Fig. 3a). The spectral signature of the factor is defined by  
303 the characteristic dominance of the  $m/z$  44 fragment, which typically serves as the primary marker for  
304 dimethylamine (DMA)-related species, closely followed by  $m/z$  58 (trimethylamine, TMA) and  $m/z$  30  
305 (methylamine, MA). This profile is in strong agreement with NOA factors resolved via PMF in other polluted

environments. For instance, the dominance of  $m/z$  44 and  $m/z$  30 aligns with amine factors reported in New York City (Sun et al., 2011) and Pasadena, California (Hayes et al., 2013). This DMA-dominated signature is also consistent with seasonal characterization of organic nitrogen in Beijing (Xu et al., 2017) and Po Valley, Italy (Saarikoski et al., 2012), reinforcing the common chemical signature of reduced organic nitrogen across diverse urban and regional environments. Furthermore, the presence of non-negligible signals at  $m/z$  58 and  $m/z$  86 supports the contribution of slightly larger alkylamines, a pattern that aligns well with established AMS laboratory reference spectra for these reduced nitrogen compounds (Ge et al., 2011; Silva et al., 2008).

These amines are commonly emitted during the combustion of nitrogen-rich biomass and proteinaceous materials and are frequently associated with biomass-burning emissions (Ge et al., 2011). Previous molecular analyses in Seoul also indicate DMA, MA, and TMA as the dominant amine species in December (Baek et al., 2022). While other amines such as triethylamine (TEA), diethylamine (DEA), and ethylamine (EA) may contribute via industrial/solvent pathways (e.g., chemical manufacturing, petrochemical corridors, wastewater treatment), our HR-AMS spectra are dominated by small alkylamine fragments ( $m/z$  30, 44, 58, 86) and the diurnal behavior covaries with combustion markers ([below Fig. 2](#)), indicating a primarily combustion-linked influence. Nevertheless, recent urban measurements and sector-based analyses show that industrial activities can contribute measurable amines in cities (Tiszenkel et al., 2024; Zheng et al., 2015; Mao et al., 2018; Shen et al., 2017; Yao et al., 2016). Accordingly, a minor NOA contribution from solvent/industrial amines cannot be excluded. [NOA exhibited a nighttime-early-morning enhancement \(Fig. 2a\), similar to BBOA, indicating that both factors are influenced by wintertime combustion and residential heating, which are known sources of small alkylamines and amides \(You et al., 2014; Yao et al., 2016\)](#). Strong correlations of NOA with  $\text{CH}_4^- \text{N}^+$  ( $r = 0.95$ ) and  $\text{C}_2^- \text{H}_6\text{N}^+$  ( $r = 0.91$ ) (Fig. 2) further support the presence of reduced-nitrogen species associated with these combustion activities. However, the time series of NOA and BBOA are not strongly correlated (Fig. 2 and Fig. S7). This contrast reflects their differing behaviors: BBOA follows a relatively regular daily emission pattern, whereas NOA appears predominantly during stagnant haze periods (Fig. 1) when cold, humid, and low-wind conditions allow semi-volatile amines to partition to the particle phase and form low-volatility aminium salts. Thus, NOA in wintertime Seoul likely reflects a combination of shared primary combustion influences and enhanced secondary processing of amine-containing precursors under meteorological conditions that favor partitioning and accumulation. Supporting this, NOA exhibited a diurnal pattern similar to that of BBOA, with both peaking at night and in the early morning (Fig. 2a), suggesting shared sources or formation mechanisms. Biomass burning under cold, oxygen limited conditions is known to emit various amines and amides (You et al., 2014; Yao et al., 2016), which may contribute directly to

336 NOA or serve as precursors for its secondary formation. Strong correlations with  $\text{CH}_3\text{N}^+$  ( $r = 0.95$ ) and  $\text{C}_2\text{H}_6\text{N}^+$  ( $r = 0.91$ ) (Fig. 2) further support the presence of reduced nitrogen compounds, typically associated with residential  
337 fuel combustion and wintertime heating. However, the time series of NOA and BBOA were not well correlated  
338 (Fig. 2 and S7), likely because NOA episodes preferentially occurred during haze periods under stagnant conditions  
339 (Fig. 1), whereas BBOA emissions tend to follow a more regular, daily emission pattern. Under cold, humid, and  
340 stagnant conditions, these semi volatile amines can readily partition into the particle phase and form low volatility  
341 aminium salts, enhancing the observed NOA signal. Taken together, these results suggest that NOA during  
342 wintertime in Seoul is strongly influenced by a combination of combustion related primary emissions and  
343 subsequent atmospheric processing of amine containing species, facilitated by seasonally favorable conditions.

344  
345 Detection of particulate NOA using real time measurement has been challenging due to its low concentration and  
346 high volatility. Although Baek et al. (2022) identified nitrogen-containing species in Seoul via year-round filter-  
347 based molecular analysis, PMF-based resolution of NOA in real time has not been previously reported. The  
348 successful identification in this study is likely attributable to favorable winter meteorological conditions—  
349 specifically low temperatures ( $-0.24^\circ\text{C}$ ) and persistently high relative humidity ( $\sim 57\%$ ) compared to the 2017  
350 winter season (Kim et al., 2017)—that enhanced gas-to-particle partitioning of semi-volatile amines, thereby  
351 enabling their detection (Fig. S2). NOA concentrations frequently exceeded  $1 \mu\text{g m}^{-3}$  when RH surpassed 60% (Fig.  
352 2), supporting the importance of RH-driven partitioning and the subsequent formation of low-volatility aminium  
353 salts (Rovelli et al., 2017). Although extremely low temperatures may inhibit NOA formation due to the transition  
354 of aerosol particles into solid phase (Ge et al., 2011; Srivastava et al., 2022), the combination of consistently cold  
355 and humid conditions during the measurement period likely promoted the partitioning of semi-volatile amines into  
356 the particle phase. In addition, episodic haze events further elevated NOA levels, increasing its contribution to OA  
357 from 1% during clean periods to as much as 3% (Fig. 1f–h). These high-concentration events likely improved the  
358 signal-to-noise ratio, facilitating PMF resolution. Back-trajectory clustering indicates that NOA-enhanced events  
359 were dominated by short-range recirculation (Cluster 1; Fig. S7), consistent with the short atmospheric lifetimes  
360 and high reactivity of alkylamines (Nielsen et al., 2012; Hanson et al., 2014). Overall, the factor reflects semi-  
361 volatile, reduced-nitrogen species originating from primary urban combustion sources, with their observed particle-  
362 phase mass amplified by rapid secondary partitioning and salt formation under seasonally favorable conditions.

363  
364

365 NOA contributed approximately 2 % of total OA, comparable to urban contributions reported in Guangzhou (3 %;  
366 Chen et al., 2021), Pasadena (5 %; Hayes et al., 2013), and New York (5.8 %; Sun et al., 2011). These similarities  
367 suggest that the NOA factor observed in Seoul reflects a broader class of urban wintertime reduced-nitrogen  
368 aerosols rather than a site-specific anomaly. In most urban environments, the detectability of NOA appears to  
369 depend strongly on the interplay between emission strength, stagnation, and humidity—which together govern the  
370 particle-phase partitioning of volatile amines.

371 atmospheric processing of amine-containing species, facilitated by seasonally favorable conditions.

### 372 3.1.2 Secondary organic aerosols (SOA)

373 In this study, two OOA factors—more oxidized OOA (MO OOA) and less oxidized OOA (LO OOA)—were  
374 identified, together accounting for approximately half of the total organic aerosol (OA) mass. This fraction is  
375 notably higher than that reported in previous wintertime urban studies (Kim et al., 2017; Zhang et al., 2007).  
376 Both OOOAs exhibited characteristic mass spectral features, including prominent peaks at  $m/z$  44 ( $\text{CO}_2^+$ ) and  $m/z$   
377 43 ( $\text{C}_2\text{H}_3\text{O}^+$ ), which are widely recognized as markers of oxygenated organics (Fig. S2e, S3f). The oxygen to  
378 carbon (O:C) ratios for MO OOA and LO OOA were 1.15 and 0.68, respectively, indicating highly oxidized  
379 chemical compositions. The O:C ratio of MO OOA was especially elevated, exceeding those reported in previous  
380 Seoul campaigns—0.68 in winter 2015 (Kim et al., 2017), 0.99 in spring 2019 (Kim et al., 2020), and 0.78 in fall  
381 2019 (Jeon et al., 2023)—while the LO OOA ratio was within a similar range.

382 MO OOA showed strong correlations with secondary inorganic species such as nitrate ( $r = 0.90$ ), ammonium ( $r = 0.92$ ),  
383 and sulfate ( $r = 0.81$ ), consistent with its formation through regional and local photochemical aging  
384 processes (Fig. S3). In contrast, LO OOA exhibited only modest correlations with sulfate, nitrate, and ammonium  
385 ( $r = 0.50$ , 0.51, and 0.42, respectively, suggesting additional contributions from semi-primary sources not closely  
386 linked to inorganic secondary formation (e.g., cooking, traffic, biomass burning). LO OOA does not exhibit a  
387 pronounced  $m/z$  60 (levoglucosan) signal (Fig. S2); however, the levoglucosan marker ( $f_{60}$ ) is known to diminish  
388 with atmospheric aging and can become weak or undetectable downwind (Hennigan et al., 2010; Cubison et al.,  
389 2011). Taken together, the weaker coupling with secondary inorganics and the absence of a strong  $m/z$  60 peak  
390 indicate that LO OOA is a mixture of aged secondary organics and semi-primary urban emissions, while a  
391 contribution from aged biomass burning influence cannot be ruled out.

### 3.1.3 Primary organic aerosols (POA)

393 Three primary organic aerosol (POA) factors were identified in this study: hydrocarbon-like OA (HOA),  
 394 cooking-related OA (COA), and biomass-burning OA (BBOA). These three components exhibited mass spectral  
 395 and temporal characteristics consistent with previous observations in Seoul and other urban environments. HOA  
 396 was characterized by dominant alkyl fragment ions ( $C_{11}H_{22}^+$  and  $C_{11}H_{20}^+$ ; Fig. S2a) and a low O:C ratio (0.13),  
 397 consistent with traffic-related emissions (0.05–0.25) (Canagaratna et al., 2015). It showed strong correlations  
 398 with vehicle-related ions  $C_3H_7^+$  ( $r = 0.79$ ) and  $C_4H_9^+$  ( $r = 0.86$ ) (Kim et al., 2017; Canagaratna et al., 2004; Zhang  
 399 et al., 2005), and exhibited a distinct morning rush hour peak (06:00–08:00), followed by a decrease likely driven  
 400 by boundary layer expansion (Fig. S3a).

401 COA, accounting for 21% of OA, showed higher contributions from oxygenated ions than HOA, with tracer  
 402 peaks at  $m/z$  55, 84 and 98 (Fig. S2b) consistent with cooking emissions (Sun et al., 2011). It correlated strongly  
 403 with cooking-related ions such as  $C_3H_7O^+$  ( $r = 0.94$ ),  $C_4H_9O^+$  ( $r = 0.96$ ), and  $C_6H_{11}O^+$  ( $r = 0.98$ ) (Fig. S3h), and  
 404 displayed prominent peaks during lunch and dinner hours, reflecting typical cooking activity patterns.

405 BBOA was identified based on characteristic ions at  $m/z$  60 ( $C_2H_2O_2^+$ ) and 73 ( $C_2H_5O^+$ ), both of which are  
 406 associated with levoglucosan – a well-established tracer for biomass burning (Simoneit et al., 2002). Its relatively  
 407 high  $f_{OC}$  and low  $f_{OC}$  values (Fig. S8a) indicate that the BBOA observed in this study was relatively fresh and had  
 408 not undergone extensive atmospheric aging (Cubison et al., 2011). Furthermore, BBOA exhibited moderate  
 409 correlations with NOA in both diurnal profiles and time series (Fig. 2), particularly with nitrogen-containing ions  
 410 such as  $C_2H_5N^+$  ( $r = 0.67$ ) and  $C_2H_6N^+$  ( $r = 0.56$ ) (Fig. 2 and S3), which are also dominant peaks in the NOA  
 411 mass spectrum. This overlap suggests a potential shared emission source or co-emission scenario, consistent  
 412 with the co-emission of both organic aerosols and reduced nitrogen-containing compounds. Regarding source  
 413 location, several pathways can influence Seoul's biomass-burning signature. First, urban/peri-urban small-scale  
 414 burning (e.g., solid fuel use in select households, restaurant charcoal use, and intermittent waste burning) has  
 415 been reported and can enhance BBOA locally (Kim et al., 2017). Second, nearby agricultural residue burning in  
 416 surrounding provinces occurs seasonally and can episodically impact the metropolitan area (Han et al., 2022).  
 417 Third, regional transport from upwind regions (e.g., northeastern China/North Korea) can bring biomass-burning  
 418 influenced air masses under northerly/northwesterly flow (Lamb et al., 2018; Nault et al., 2018). In this dataset,  
 419 the nighttime and early morning enhancements, the BBOA–NOA co-variation, and trajectory clusters showing

420 regional recirculation indicate a predominantly local/near source contribution during the study period (Yoo et al.,  
421 2024), with episodic non-local influences remaining possible.

## 422 3.2 Volatility of Non-Refractory Species

423 Figure 4 presents thermograms of non-refractory (NR) species measured by HR-ToF-AMS. The mass fraction  
424 remaining (MFR) after thermodenuder (TD) treatment follows the typical volatility trend reported in previous  
425 studies (Xu et al., 2016; Kang et al., 2022; Jeon et al., 2023; Huffman et al., 2009): nitrate was the most volatile,  
426 followed by chloride, ammonium, organics, and sulfate. Nitrate showed the steepest decline with increasing  
427 temperature, with a  $T_{50}$  of  $\sim 67$  °C—substantially higher than that of pure ammonium nitrate ( $\sim 37$  °C; Huffman  
428 et al., 2009). At 200 °C,  $\sim 2\%$  of the initial nitrate signal remained (Fig. 4). Since pure ammonium nitrate fully  
429 evaporates well below this temperature (Huffman et al., 2009), this small residual fraction likely represents the  
430 least volatile portion of organic nitrates. Nitrate showed the steepest decline with temperature, with a  $T_{50}$  of  
431  $\sim 67$  °C higher than pure ammonium nitrate ( $\sim 37$  °C; Huffman et al., 2009), suggesting contributions from less  
432 volatile species like organonitrates or metal nitrates (Feng et al., 2023). This small residual mass is consistent  
433 with previous observations of thermally refractory or semi-refractory nitrate species—including organonitrates  
434 with low effective saturation concentrations and nitrate associated with transition metal ions—which are  
435 incompletely vaporized in AMS instruments (Farmer et al., 2010; Xu et al., 2015; Canagaratna et al., 2007). As  
436 AMS cannot directly distinguish between inorganic and organic nitrate at high TD temperatures, this residual  
437 fraction reflects low volatility nitrate-containing material rather than ammonium nitrate itself. Nearly complete  
438 evaporation occurred by 200 °C ( $\sim 2\%$  remaining). Compared to previously reported fall conditions ( $T_{50} \sim 73$  °C,  
439 incomplete evaporation), winter nitrate appeared more volatile, indicating relatively fewer non-volatile nitrate  
440 forms (e.g., Kang et al., 2022; Jeon et al., 2023). Sulfate exhibited the highest thermal stability among the  
441 measured species. The thermogram showed a relatively stable mass fraction (MFR  $> 0.8$ ) up to  $\sim 130$  °C, followed  
442 by a sharp decline at temperatures above 140 °C (Fig. 4). This profile is consistent with the typical volatilization  
443 behavior of ammonium sulfate in TD-AMS, which requires higher temperatures to evaporate compared to nitrate  
444 or organics (Huffman et al., 2009). At 200 °C, approximately 25% of the sulfate mass remained. This residual  
445 suggests the presence of a sulfate fraction with lower volatility than pure ammonium sulfate, likely associated  
446 with organosulfates or low-volatility mixtures, whereas refractory metal sulfates are not efficiently detected by  
447 the AMS (Canagaratna et al., 2007). Sulfate was the least volatile ( $T_{50} \approx 170$  °C), consistent with ammonium  
448 sulfate (Scott and Cattell, 1979). A subtle slope change near 140 °C likely reflects ammonium sulfate

449 morphology or phase state changes and/or interactions between organosulfate and inorganic mixingsulfate,  
450 rather than contributions from metallic (refractory) sulfates, which are not efficiently detected by AMS (Huffman  
451 et al., 2009; Canagaratna et al., 2007). Approximately 25% of the initial sulfate signal remained at 200 °C (Fig.  
452 4), suggesting the presence of low volatility sulfate-containing material or mixed organic inorganic components,  
453 although the AMS alone cannot resolve their specific chemical identity. About 25% remained at 200 °C,  
454 indicating possible contributions from metallic or organic sulfates. Ammonium showed intermediate volatility,  
455 with  $T_{50}$  between nitrate and sulfate. Its slightly lower winter  $T_{50}$  suggests stronger nitrate association. Residual  
456 ammonium at 200 °C was consistent (~4%) in previously reported spring/fall measurements (Kang et al., 2022;  
457 Jeon et al., 2023). Chloride volatility was broadly consistent with prior AMS studies, with  $T_{50}$  values comparable  
458 across seasons (e.g., Xu et al., 2016; Jeon et al., 2023). The near-complete evaporation observed in winter (~4%  
459 residual at 200 °C, Fig. 4) indicates that the chloride measured here was dominated by volatile inorganic chloride,  
460 specifically ammonium chloride ( $\text{NH}_4\text{Cl}$ ), which fully evaporates at relatively low temperatures (Huffman et al.,  
461 2009). By contrast, metal chlorides (e.g.,  $\text{NaCl}$ ,  $\text{KCl}$ ) are refractory and far less volatile; they are also poorly  
462 detected by the AMS (Canagaratna et al., 2007). The lower residual in winter compared to fall (~10%) therefore  
463 suggests that wintertime chloride consisted almost exclusively of pure ammonium chloride, whereas the fall  
464 samples may have contained a minor fraction of less volatile or refractory chloride species. “Chloride volatility  
465 was broadly consistent with prior AMS studies, with  $T_{50}$  values comparable across seasons (e.g., Xu et al., 2016;  
466 Jeon et al., 2023). The near complete evaporation observed in winter (~4% residual at 200 °C, Fig. 4) suggests  
467 that the chloride measured here was dominated by volatile inorganic chloride, such as ammonium chloride  
468 ( $\text{NH}_4\text{Cl}$ ), which fully evaporates at relatively low temperatures (Huffman et al., 2009; Middlebrook et al., 2012).  
469 By contrast, metal chlorides (e.g.,  $\text{NaCl}$ ,  $\text{KCl}$ ) are far less volatile and are poorly detected by AMS due to their  
470 refractory nature (Canagaratna et al., 2007). The lower winter residual compared to fall (~10%) therefore likely  
471 reflects a shift toward more volatile chloride sources—such as residential heating or road salt-related  $\text{NH}_4\text{Cl}$   
472 formation—rather than contributions from refractory metal chlorides. Chloride volatility was also comparable  
473 across seasons in prior studies in terms of  $T_{50}$ , but exhibited more complete evaporation in winter (~4% residual  
474 vs. ~10% in fall), possibly reflecting a shift in source to more volatile forms like road salt during wintertime.  
475 Organics exhibited moderate volatility ( $T_{50} \sim 120$  °C), and their thermogram showed a gradual, continuous  
476 decrease in mass fraction with increasing TD temperature. This smooth profile reflects the presence of a broad  
477 distribution of organic compounds spanning SVOC to LVOC ranges, in contrast to inorganic species such as  
478 nitrate or ammonium chloride, which often show more abrupt losses at characteristic temperatures (Huffman et  
479 al., 2009; Xu et al., 2016). This behavior is consistent with previous TD-AMS observations in Seoul during

480 spring and fall (Kang et al., 2022; Jeon et al., 2023). Organics exhibited moderate volatility ( $T_{50} \sim 120^\circ\text{C}$ ), and  
481 their thermogram showed a gradual, continuous decrease in mass fraction with increasing TD temperature. This  
482 smooth profile reflects the presence of a broad distribution of organic compounds spanning SVOC to LVOC  
483 ranges, in contrast to inorganic species such as nitrate or ammonium chloride, which often show more abrupt  
484 losses at characteristic temperatures (Huffman et al., 2009; Xu et al., 2016). This behavior is consistent with  
485 previous TD-AMS observations in Seoul during spring and fall (Kang et al., 2022; Jeon et al., 2023). OA  
486 exhibited moderate volatility ( $T_{50} \sim 120^\circ\text{C}$ ), consistent with the presence of a wide variety of compounds with  
487 differing volatilities. This trend aligns with previously reported spring and fall observations in Seoul, Korea  
488 (Kang et al., 2022; Jeon et al., 2023).

489  
490

### 491 3.2.1 Volatility Profiles of Organic sources

492 Figure 5 presents the volatility distributions of six OA sources within the volatility basis set (VBS) framework.  
493 Volatility is expressed as the effective saturation concentration ( $C^*$ ,  $\mu\text{g m}^{-3}$ ), where higher  $C^*$  values correspond  
494 to higher volatility. Following Donahue et al. (2009),  $C^*$  values are categorized into four bins: extremely low-  
495 volatility organic compounds (ELVOCs,  $\log C^* < -4.5$ ), low-volatility organic compounds (LVOCs,  $-4.5 < \log$   
496  $C^* < -0.5$ ), semi-volatile organic compounds (SVOCs,  $-0.5 < \log C^* < 2.5$ ), and intermediate-volatility organic  
497 compounds (IVOCs,  $2.5 < \log C^* < 6.5$ ).

498 Among the primary OA (POA) sources, hydrocarbon-like OA (HOA) exhibited the highest volatility, with mass  
499 predominantly distributed in the SVOC and IVOC ranges, consistent with its chemically reduced nature (O:C =  
500 0.13) and direct combustion origin. Mass fraction remaining (MFR) results (Fig. S9) further support this, showing  
501 rapid mass loss at lower temperatures. Biomass burning OA (BBOA) and nitrogen-containing OA (NOA) also  
502 showed high volatility, peaking in the SVOC–IVOC range ( $\log C^* = 1–3$ ), but displayed slightly higher O:C ratios  
503 (0.25 and 0.19, respectively). This modest enhancement in O:C reflects their source composition—biomass  
504 combustion produces partially oxygenated organic species (e.g., levoglucosan, phenols), and NOA contains  
505 nitrogen-bearing functional groups—rather than enhanced atmospheric oxidation. Among the primary OA (POA)  
506 sources, hydrocarbon-like OA (HOA) exhibited the highest volatility, with mass predominantly distributed in the  
507 SVOC and IVOC ranges. This is consistent with its low oxidation state (O:C = 0.35) and primary emission  
508 characteristics. Mass fraction remaining (MFR) results (Fig. S9) further support this, showing rapid mass loss at

509 lower temperatures. Biomass burning OA (BBOA) and nitrogen-containing OA (NOA) also showed high volatility,  
510 peaking in the SVOC–IVOC range ( $\log C^* = 1\text{--}3$ ), and had lower O:C ratios of 0.25 and 0.19, respectively. Their  
511 slightly more oxidized nature relative to HOA, despite a similar volatility range, may reflect emissions occurring  
512 under nighttime or cooler conditions, which promote condensation of otherwise volatile species. The similar  
513 volatility distributions and MFR profiles of BBOA and NOA (Fig. S9) further support the possibility of a shared  
514 emission source or formation pathway (Section 3.1.1). Cooking-related OA (COA) showed a more moderate  
515 volatility profile, with mass more evenly distributed across the LVOC and SVOC bins. This behavior differs from  
516 that of BBOA, which is slightly more oxidized yet more volatile. This apparent decoupling between oxidation state  
517 and volatility is a characteristic feature of COA reported in previous volatility studies (Paciga et al., 2016; Kang et  
518 al., 2022). These studies attribute the lower volatility of COA to its abundance of high-molecular-weight fatty acids  
519 (e.g., oleic, palmitic, and stearic acids) and glycerides (Mohr et al., 2009; He et al., 2010). Unlike the smaller,  
520 fragmented molecules typical of biomass burning, these lipid-like compounds possess high molar masses that  
521 suppress volatility, even though their long alkyl chains result in low O:C ratios.

522 Cooking-related OA (COA) showed a more moderate volatility profile, with mass more evenly distributed across  
523 the LVOC and SVOC bins. This pattern reflects its diverse cooking sources and variable emission profiles as  
524 previously reported (Kang et al., 2022)..

525 For secondary OA (SOA), less-oxidized oxygenated OA (LO-OOA) exhibited the lowest volatility, with substantial  
526 mass in the LVOC and ELVOC bins ( $C^* \approx 10^{-3}\text{--}10^{-4}$ ). This is in agreement with previous findings in Seoul during  
527 spring (Kang et al., 2022). In contrast, more-oxidized OOA (MO-OOA), despite its higher oxidation state (O:C =  
528 1.15), displayed greater volatility, with a peak at  $C^* \approx 10^1$ . This discrepancy likely reflects differences in formation  
529 and aging processes, as discussed further in Section 3.3.

530 Overall, the volatility characteristics across OA factors suggest that oxidation state alone does not fully explain  
531 volatility. Rather, volatility is shaped by a combination of emission source, emission timing, temperature, and  
532 atmospheric processing. These findings highlight the importance of integrating both chemical and physical  
533 characterization to better understand OA formation and aging across seasons.

### 534 3.3 Aging effect on volatility from 2D VBS

535 Generally, the oxygen-to-carbon (O:C) ratio of organic aerosols (OA) is inversely related to their volatility. As O:C  
536 increases through aging, the effective saturation concentration ( $C^*$ ) typically decreases, resulting in lower volatility

537 (Donahue et al., 2006; Jimenez et al., 2009). This relationship arises because oxidative functionalization introduces  
538 polar groups (e.g., hydroxyl, carboxyl) that increase molecular weight and enhance intermolecular hydrogen  
539 bonding, thereby reducing the effective saturation concentration ( $C^*$ ) and promoting particle-phase retention  
540 (Jimenez et al., 2009; Kroll and Seinfeld, 2008; Donahue et al., 2011). This common relationship arises because  
541 the addition of oxygen-containing functional groups (e.g., hydroxyl, carboxyl, carbonyl), which increases molecular  
542 weight and enhances intermolecular interactions such as hydrogen bonding, thereby reducing vapor pressure  
543 (Jimenez et al., 2009; Kroll and Seinfeld, 2008). Moreover, oxidative aging often leads to oligomerization or  
544 functionalization, promoting particle-phase retention and reducing the effective saturation concentration ( $C^*$ )  
545 (Donahue et al., 2011; Robinson et al., 2007). However, in this study, the most oxidized OA factor—MO-OOA,  
546 with a high O:C ratio of 1.15—exhibited unexpectedly high volatility. Its volatility distribution was skewed toward  
547 SVOCs and IVOCs (Fig. 5), and its rapid mass loss in MFR thermograms (Fig. S9) further indicated low thermal  
548 stability. This observation appears to contradict the usual inverse O:C–volatility relationship; however, under  
549 winter haze conditions—with suppressed  $O_3$ /low OH, particle-phase autoxidation and fragmentation can yield  
550 higher-O:C yet more volatile products, with enhanced condensation on abundant particle surface area (details  
551 below).

552 Viewed against prior TD-AMS results, the volatility of Seoul's winter MO-OOA presents a unique case,  
553 particularly in the nature of its O:C–volatility relationship. Prior urban studies have commonly reported substantial  
554 SVOC-OA, consistent with high photochemical activity or elevated loadings; for example, prior TD-AMS studies  
555 in Mexico City, Los Angeles, Beijing, and Shenzhen have all reported substantial SVOC–IVOC contributions  
556 during polluted periods, indicating that high OA volatility is a common feature of urban environments across  
557 seasons (Cappa and Jimenez, 2010; Xu et al., 2019; Cao et al., 2018)Mexico City/Los Angeles showed pronounced  
558 SVOC–IVOC contributions during warm seasons (Cappa and Jimenez, 2010), and summertime Beijing and  
559 wintertime Shenzhen likewise exhibited strong overall OA volatility (Xu et al., 2019; Cao et al., 2018). While these  
560 comparisons establish that volatile OA is common, they generally did not report the factor-level inversion observed  
561 here, where the highly-oxidized OOA component (MO-OOA) was more volatile than a less-oxidized OOA (LO-  
562 OOA). This behavior is distinct from findings in colder, lower-loading regimes; wintertime Paris, for instance,  
563 maintained the conventional hierarchy where the more-oxidized OOA was comparatively less volatile (Paciga et  
564 al., 2016). Furthermore, seasonal context within Seoul showed springtime OA with lower oxidation levels than our  
565 winter MO-OOA despite similar SVOC contributions (Kang et al., 2022). This comprehensive comparison

566 underscores the unusual nature of the O:C-volatility relationship observed under the specific winter haze conditions  
567 in Seoul.

568

569 **3.3.1 High-volatility nature of MO-OOA in Seoul wintertime**

570 MO-OOA exhibited high O:C ratios and high apparent volatility, characteristics that were further amplified during  
571 haze episodes—periods marked by reduced ozone levels, low solar radiation, and elevated aerosol mass  
572 concentrations (Fig. 67 and Fig. S6, yellow shading). Spectrally, MO-OOA was defined by a consistently high  $f_{44}$   
573 ( $\text{CO}_2^+$ ) signal and a comparatively stable  $f_{43}$  ( $\text{C}_2\text{H}_3\text{O}^+$ ) signal relative to LO-OOA (Fig. S8b6). Notably, when MO-  
574 OOA concentrations intensified during haze, only  $f_{44}$  was significantly enhanced, while  $f_{43}$  remained nearly  
575 unchanged (Fig. 6). This trend is corroborated by the haze–non-haze comparison (Fig. S12), where haze periods  
576 (including high MO-OOA intervals) showed elevated contributions from oxygenated fragments ( $m/z$  28, 29, 44)  
577 and higher O:C ratios. In contrast, non-haze periods were characterized by larger fractional contributions from  
578 hydrocarbon-like fragments ( $m/z$  41, 43, 55, 57). The observed temporal pattern—elevated  $f_{44}$  without  
579 corresponding changes in  $f_{43}$ —is a typical signature of highly oxidized and fragmented organic aerosol (Figs. 6 and  
580 7), suggesting that aging was dominated by fragmentation rather than functionalization (Kroll et al., 2009). These  
581 spectral patterns collectively indicate that MO-OOA is highly oxidized yet remains relatively volatile compared to  
582 LO-OOA.

583 The elevated volatility of MO-OOA despite its high O:C (~1.15) indicates that oxidation under these haze  
584 conditions did not follow the classical multi-generational OH-driven aging pathway, which typically increases  
585 molecular mass and reduces volatility. Instead, the data align with fragmentation-dominated aging, where highly  
586 oxygenated but lower-molecular-weight compounds (e.g., small acids or diacids) are formed. Prior field and  
587 laboratory studies using online AMS/FIGAERO-CIMS and EESI-TOF have similarly reported high-O:C yet  
588 volatile product distributions characterized by high  $f_{44}$  and stable  $f_{43}$  (Kroll et al., 2009; Ng et al., 2010; Chhabra et  
589 al., 2011; Lambe et al., 2012; Lopez-Hilfiker et al., 2016; D’Ambro et al., 2017).

590 While direct mechanistic measurements were not available in this study, we hypothesize that the formation of this  
591 volatile, high-O:C component may be driven by specific low-light oxidation pathways consistent with the observed  
592 environmental conditions. The suppressed ozone levels during haze likely indicate a low-OH oxidation regime (Fig.  
593 67). Under such conditions, radical chemistry involving  $\text{NO}_3$  (which is longer-lived in low light) or particle-phase  
594 autoxidation could preferentially produce highly oxygenated but relatively small organic fragments (Ehn et al.,

595 2014; Zhao et al., 2023). Although haze suppresses photolysis, HONO concentrations—maintained via  
596 heterogeneous conversion or surface emissions—could still provide a non-negligible source of OH (Gil et al., 2021;  
597 Kim et al., 2024; Slater et al., 2020). Furthermore, the high aerosol mass loadings during haze ( $C_{oa}$ ) provide  
598 abundant surface area for absorptive partitioning (Pankow, 1994; Donahue et al., 2006). This increased partitioning  
599 mass allows even relatively volatile, oxidized compounds to condense into the particle phase, contributing to the  
600 high apparent volatility and oxidation state observed (Jimenez et al., 2009; Ng et al., 2016). Consequently, these  
601 results underscore the need for SOA models to incorporate fragmentation-dominated pathways to accurately  
602 represent wintertime haze evolution.

603 **Proposed Mechanism: Fragmentation and Condensation under Low OH Haze**

604 ~~MO OOA concentrations increased during haze episodes—characterized by reduced ozone levels, low solar  
605 radiation and elevated aerosol mass concentrations (Fig. 6 and Fig. S6, yellow shading). high  $f_{4+}$  ( $CO_2^+$ ) MO  
606 OOA in this study was characterized by a consistently high  $f_{4+}$  ( $CO_2^+$ ) signal and a relatively stable  $f_{4+}$  ( $C_2H_5O^+$ )  
607 signal compared to LO OOA (Fig. S8b). During specific periods when MO OOA concentrations increased,  
608 only  $f_{4+}$  was noticeably enhanced, while  $f_{4+}$  remained flat (Fig. 6). This temporal pattern—elevated  $f_{4+}$  without  
609 corresponding changes in  $f_{4+}$ —is a typical signature of highly oxidized and fragmented organic aerosol and  
610 suggests advanced aging dominated by fragmentation rather than functionalization (Kroll et al., 2009).  
611 Consistent with this, the haze–non haze comparison, including the high MO OOA interval (Fig. S12), shows  
612 larger oxygenated fragments ( $m/z$  28, 29, 44) and higher  $f_{4+}$  and O:C during haze, whereas non haze periods  
613 exhibit relatively larger fractional hydrocarbon fragments ( $m/z$  41, 43, 55, 57). Unlike classical OH initiated,  
614 multi-generational aging—which increases molecular mass and reduces volatility—fragmentation dominated  
615 oxidation can cleave larger precursors into smaller oxygenated compounds, resulting in higher volatility  
616 despite elevated O:C. Consistent with this interpretation, online AMS/FIGAERO CIMS and EESI TOF, as  
617 well as offline HRMS/GC MS, have reported high O:C yet more volatile product distributions accompanied  
618 by elevated  $f_{4+}$  with comparatively stable  $f_{4+}$  under fragmentation dominated aging (Kroll et al., 2009; Ng et al.,  
619 2010; Chhabra et al., 2011; Lambe et al., 2012; Lopez Hilfiker et al., 2016; D’Ambro et al., 2017). Furthermore,  
620 high aerosol mass loadings during haze events provide abundant surface area for the uptake of semi-  
621 volatile/intermediate volatility organics via absorptive partitioning, so that higher  $C_{oa}$  enhances condensation  
622 (Pankow, 1994; Donahue et al., 2006; Hallquist et al., 2009; Robinson et al., 2007). We also note that  
623 **functionalized, low molecular weight compounds can reside in the SVOC–IVOC range and thus contribute**  
624 **to the high apparent volatility of MO OOA (Ng et al., 2010; Chhabra et al., 2011; Lopez Hilfiker et al., 2016;**~~

625 D'Ambro et al., 2017). . This facilitates the condensation of even relatively volatile, oxidized compounds onto  
626 particles (Fig. 6). The net result is an apparent increase in both oxidation state and volatility of OA, as reported  
627 in aging studies under stagnant and polluted conditions (Jimenez et al., 2009; Ng et al., 2016).  
628 The suppressed ozone likely indicates lower OH radical production via O<sub>3</sub> photolysis, leading to a low OH  
629 oxidation regime. We note that haze also suppresses HONO photolysis; however, HONO concentrations can be  
630 elevated at night and early morning via heterogeneous NO<sub>2</sub> conversion and surface emissions, so net OH from  
631 HONO may remain non-negligible even as photolysis rates are depressed (e.g., Gil et al., 2021; Kim et al., 2024;  
632 Slater et al., 2020). Under such conditions, particle phase autoxidation involving RO<sub>2</sub> radicals can become the  
633 dominant oxidation pathway. Even under low OH conditions, NO<sub>3</sub> formed via NO<sub>2</sub> + O<sub>3</sub> can initiate RO<sub>2</sub>  
634 production through addition to alkenes, while reduced photolysis at night/low light extends NO<sub>3</sub> lifetimes; these  
635 RO<sub>2</sub> then participate in particle phase autoxidation, yielding highly oxygenated yet relatively volatile products.  
636 These processes tend to produce highly oxidized but relatively low molecular weight products (Ehn et al., 2014;  
637 Zhao et al., 2023). Unlike classical OH initiated, multi-generational aging – which increases molecular mass and  
638 reduces volatility – fragmentation dominated oxidation can cleave larger precursors into smaller oxygenated  
639 compounds, resulting in higher volatility despite elevated O:C. Consistent with this interpretation, online  
640 AMS/FIGAERO CIMS and EESI-TOF, as well as offline HRMS/GC-MS, have reported high O:C yet more  
641 volatile product distributions accompanied by elevated  $f_{\text{H}}$  with comparatively stable  $f_{\text{H}}$  under fragmentation-  
642 dominated aging (Kroll et al., 2009; Ng et al., 2010; Chhabra et al., 2011; Lambe et al., 2012; Lopez-Hilfiker et  
643 al., 2016; D'Ambro et al., 2017). Furthermore, high aerosol mass loadings during haze events provide abundant  
644 surface area for the uptake of semi-volatile/intermediate-volatility organics via absorptive partitioning, so that  
645 higher C<sub>OA</sub> enhances condensation (Pankow, 1994; Donahue et al., 2006; Hallquist et al., 2009; Robinson et al.,  
646 2007). We also note that functionalized, low molecular weight compounds can reside in the SVOC-IVOC range  
647 and thus contribute to the high apparent volatility of MO-OOA (Ng et al., 2010; Chhabra et al., 2011; Lopez-  
648 Hilfiker et al., 2016; D'Ambro et al., 2017). . This facilitates the condensation of even relatively volatile, oxidized  
649 compounds onto particles (Fig. 6). The net result is an apparent increase in both oxidation state and volatility of  
650 OA, as reported in aging studies under stagnant and polluted conditions (Jimenez et al., 2009; Ng et al., 2016).  
651 In line with these reports, our results also revealed a decoupling between O:C and volatility, with MO-OOA  
652 showing high volatility despite its elevated O:C ratio (~1.15). While this behavior has been observed in other  
653 urban environments, this study provides one of the first detailed thermodynamic assessments of this decoupling  
654 under winter haze conditions in Seoul using real-time TD-AMS measurements. Supporting this interpretation,

655 MO-OOA in this study was characterized by a consistently high  $f_{\text{MO}}(\text{CO}_2^+)$  signal and a relatively stable  $f_{\text{MO}}(\text{C}_2\text{H}_5\text{O}^+)$  signal compared to LO-OOA (Fig. S8b). During specific periods when MO-OOA concentrations 656 increased, only  $f_{\text{MO}}$  was noticeably enhanced, while  $f_{\text{LO}}$  remained flat (Fig. 6). This temporal pattern elevated  $f_{\text{MO}}$  657 without corresponding changes in  $f_{\text{LO}}$  is a typical signature of highly oxidized and fragmented organic aerosol 658 and suggests advanced aging dominated by fragmentation rather than functionalization (Kroll et al., 2009). 659 Consistent with this, the haze/non-haze comparison, including the high MO-OOA interval (Fig. S12), shows larger 660 oxygenated fragments ( $m/z$  28, 29, 44) and higher  $f_{\text{MO}}$  and O:C during haze, whereas non-haze periods exhibit relatively larger 661 fractional hydrocarbon fragments ( $m/z$  41, 43, 55, 57). These spectral contrasts indicate that the elevated volatility of MO- 662 OOA reflects advanced oxidation via autoxidation and the condensation of small oxygenated fragments rather than 663 enrichment of high-molecular-weight ions, particularly under conditions of limited OH and high particulate surface area. 664

665 This unexpected volatility behavior of highly oxidized MO-OOA highlights the need for secondary organic 666 aerosol (SOA) models to incorporate fragmentation-dominated oxidation pathways especially under haze 667 conditions where conventional assumptions linking O:C to volatility may break down. Including such 668 mechanisms could improve model accuracy in representing OA aging and volatility in urban air quality 669 simulations.

## 670 4 Conclusions

671 This study provides a comprehensive characterization of wintertime submicron aerosols (PM<sub>1</sub>) in Seoul, integrating 672 chemical composition, volatility measurements, and source apportionment to reveal critical insights into urban OA 673 evolution. The two most significant findings are the robust real-time identification of a nitrogen-containing organic 674 aerosol (NOA) factor and the observation of unexpected volatility behavior in highly oxidized OA. The NOA factor, 675 spectrally dominated by low-molecular-weight alkylamine fragments, was successfully resolved primarily due to 676 the accumulation of pollutants during wintertime stagnation, which sufficiently enhanced the spectral signals of 677 these semi-volatile species for identification. Its temporal and chemical characteristics point to a mixed 678 primary/secondary origin: driven by direct combustion emissions (e.g., residential heating) but significantly 679 enhanced by the rapid gas-to-particle partitioning of semi-volatile amines under cold, humid conditions. 680 Concurrently, the volatility analysis revealed a striking decoupling between oxidation state and volatility for the 681 More-Oxidized Oxygenated OA (MO-OOA). Despite its high O:C ratio (~1.15), MO-OOA exhibited elevated 682 volatility, a deviation from classical aging models that typically associate high oxidation with low volatility. This 683 behavior is attributed to the specific conditions of winter haze—reduced photolysis and high aerosol mass

684 loadings—which favor fragmentation-dominated aging pathways and the absorptive partitioning of volatile  
685 oxygenated products.

686 These results revise our understanding of wintertime aerosol dynamics and underscore the limitations of current  
687 models in representing reduced-nitrogen species and non-canonical oxidation pathways. To address the  
688 remaining uncertainties, future research should prioritize evaluating the seasonal variability of NOA to better  
689 disentangle the influence of meteorological drivers from specific emission sources. Concurrently, there is a  
690 critical need to directly probe radical oxidation mechanisms, such as RO<sub>2</sub> autoxidation and NO<sub>3</sub> chemistry,  
691 particularly under haze conditions. Integrating these field inquiries with laboratory studies and advanced  
692 molecular-level measurements (e.g., FIGAERO-CIMS, EESI-TOF) will be essential for constraining the  
693 formation, lifetime, and climate impacts of these complex organic aerosol components in polluted  
694 megacities.These results revise our understanding of wintertime aerosol dynamics and underscore the limitations  
695 of current models in representing reduced nitrogen species and non canonical oxidation pathways. To address  
696 the remaining uncertainties, future research should focus on three key areas: (1) evaluating the seasonal  
697 variability of NOA to disentangle the influence of meteorological drivers from specific emission sources; (2)  
698 quantifying the specific roles of heterogeneous reactions and aminium salt formation in NOA persistence; and  
699 (3) directly probing radical oxidation mechanisms (e.g., RO<sub>2</sub> autoxidation, NO<sub>3</sub> chemistry) under haze conditions.  
700 Combining these field inquiries with laboratory studies and advanced molecular level measurements (e.g.,  
701 FIGAERO-CIMS, EESI-TOF) will be essential for constraining the formation, lifetime, and climate impacts of  
702 these complex organic aerosol components in polluted megacities.

703 This study offers a detailed characterization of wintertime submicron aerosols (PM<sub>1</sub>) in Seoul by integrating  
704 chemical composition, volatility behavior, and source apportionment to better understand their formation and  
705 atmospheric evolution. Organic aerosols (OA), particularly secondary organic aerosols (SOA), were the  
706 dominant PM<sub>1</sub> component, highlighting the significance of oxidative processes even during cold seasons. A  
707 notable result is the successful real time resolution of a nitrogen containing organic aerosol (NOA) factor,  
708 enabled by cold, humid meteorological conditions that enhanced the partitioning and stabilization of amine-  
709 derived compounds. The NOA factor was characterized by tracer ions associated with low molecular weight  
710 alkylamines such as TMA, DMA, and MA, which likely originated from biomass combustion.

712 Volatility analysis revealed distinct thermodynamic behavior across OA sources. Primary OA factors such as  
713 HOA, BBOA, and COA exhibited relatively high volatility, while LO-OOA showed low volatility and a higher  
714 oxidation state, consistent with aged, low volatility material. The similarity in volatility distributions and  
715 diurnal patterns between BBOA and NOA suggests that biomass combustion under wintertime conditions is a  
716 likely contributor to both primary organic and nitrogenous aerosol formation.

717

718 Interestingly, MO-OOA—despite its high oxygen to carbon (O:C) ratio—exhibited elevated volatility, diverging  
719 from the expected inverse relationship between oxidation state and volatility. This suggests that under stagnant,  
720 polluted conditions with suppressed ozone and OH radical levels, particle phase autoxidation and fragmentation  
721 pathways may dominate over traditional OH initiated aging, yielding highly oxidized yet semi-volatile products.  
722 These findings highlight the importance of coupling high resolution chemical and physical aerosol measurements  
723 to better understand OA formation processes and properties within urban air quality frameworks. Consequently,  
724 air quality models should incorporate diverse oxidation mechanisms and avoid assuming a direct link between  
725 oxidation state and volatility.

726 **Data availability.**

727 Data presented in this article are available upon request to the corresponding author.

728 **Acknowledgements**

729 This work was supported by the National Research Foundation of Korea (NRF) grant funded by the Korea government (MSIT)  
730 (RS-2025-00514570), the project “development of SMaRT based aerosol measurement and analysis systems for the evaluation  
731 of climate change and health risk assessment” operated by Seoul National University (900-20240101).

732 **Author Contributions**

733 Hwajin Kim designed and prepared the manuscript. Jiwoo Jeong operated the TD-AMS and analyse the data. Jihye Moon  
734 analyse the data. Hyungu Kang analyse the volatility of OA.

735

736 **Competing interests.**

737 The authors declare that they have no conflict of interest.

738

739

740

741

742

743

744

745

746

747

748

749

750

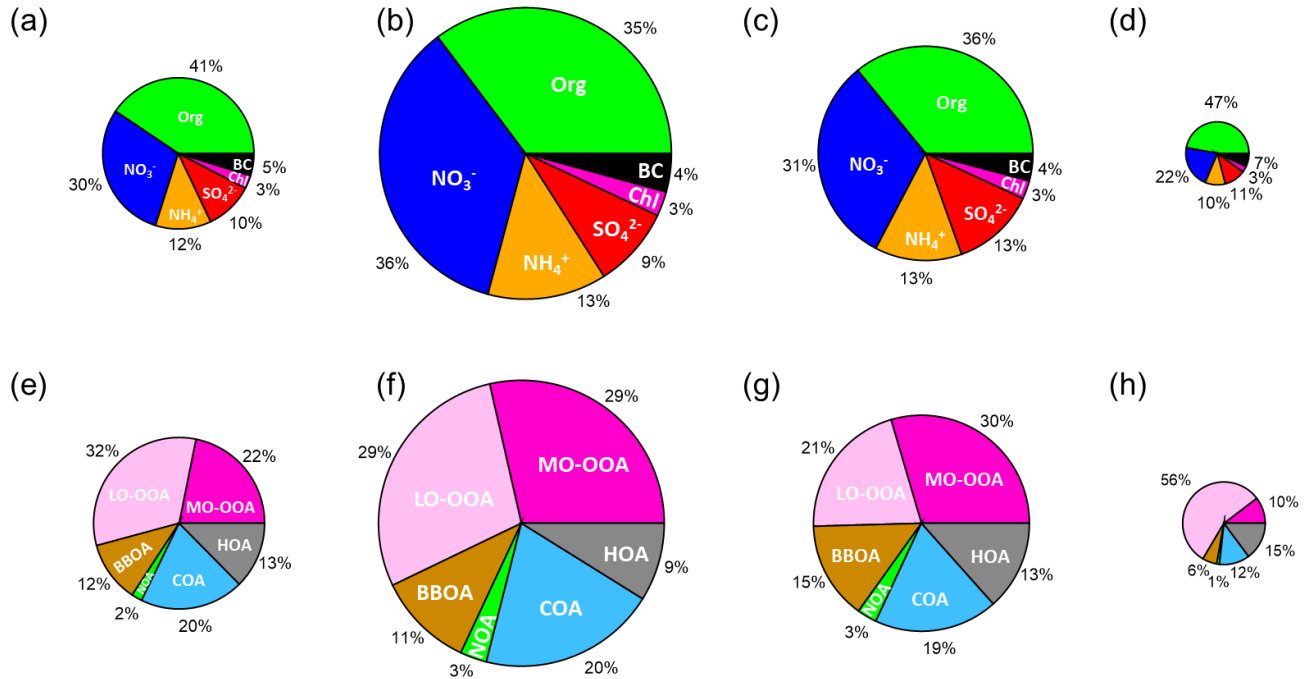
751

752

753

754

755

756  
757758 **Tables and Figures**759  
760  
761

762

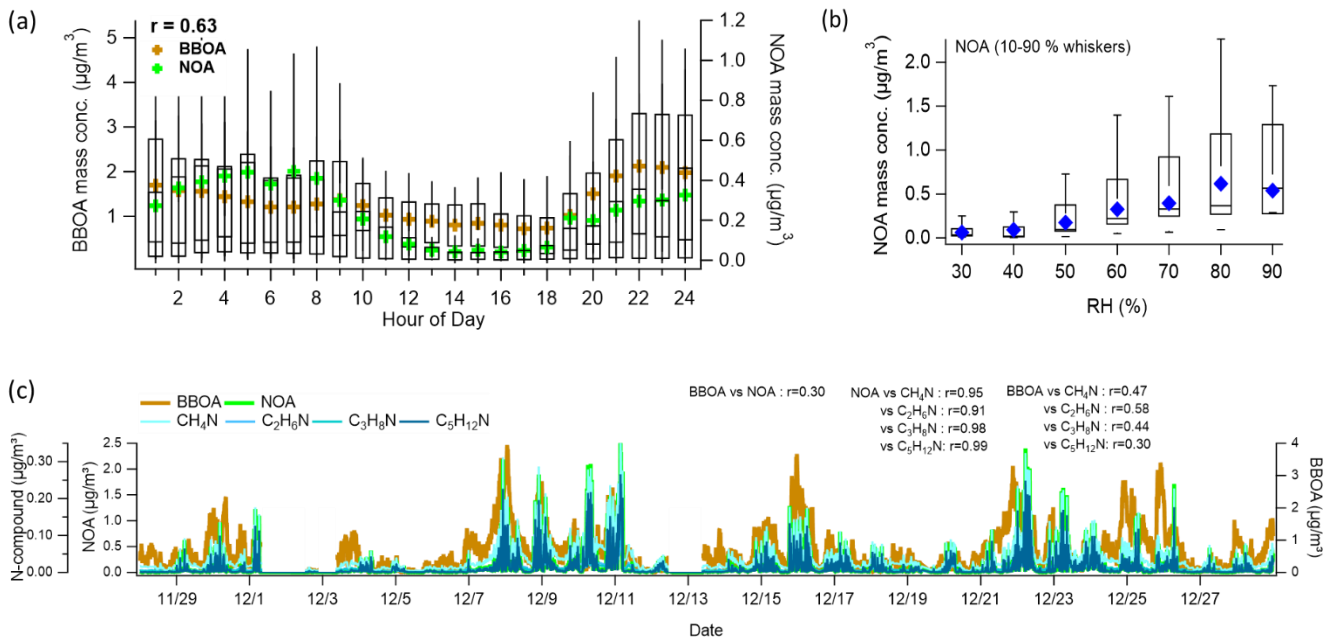
	Period	Standard	Avg. Mass conc. ( $\mu\text{g m}^{-3}$ )
<b>Total</b>	2019.11.28 ~ 2019.12.28		Avg $\text{PM}_1 = 26.37$
<b>Clean</b>	2019.12.04 ~ 2019.12.06	Daily $\text{PM}_1 < 10.00 \mu\text{g m}^{-3}$	Avg $\text{PM}_1 = 9.98$
<b>Haze 1</b>	2019.12.07 ~ 2019.12.11	Daily $\text{PM}_1 > 30.00 \mu\text{g m}^{-3}$	Avg $\text{PM}_1 = 51.88$
<b>Haze 2</b>	2019.12.21 ~ 2019.12.25	Daily $\text{PM}_1 > 30.00 \mu\text{g m}^{-3}$	Avg $\text{PM}_1 = 37.71$

763  
764  
765  
766  
767

**Figure 1.** Compositional pie charts of  $\text{PM}_1$  species for (a) the entire study period, (b) haze period 1, (c) haze period 2, and (d) a clean period; and of each OA source for (e) the entire study period, (f) haze period 1, (g) haze period 2, and (h) the clean period. Table. Standard and average  $\text{PM}_1$  mass concentrations during the entire study period, haze period 1, haze period 2, and the clean period.

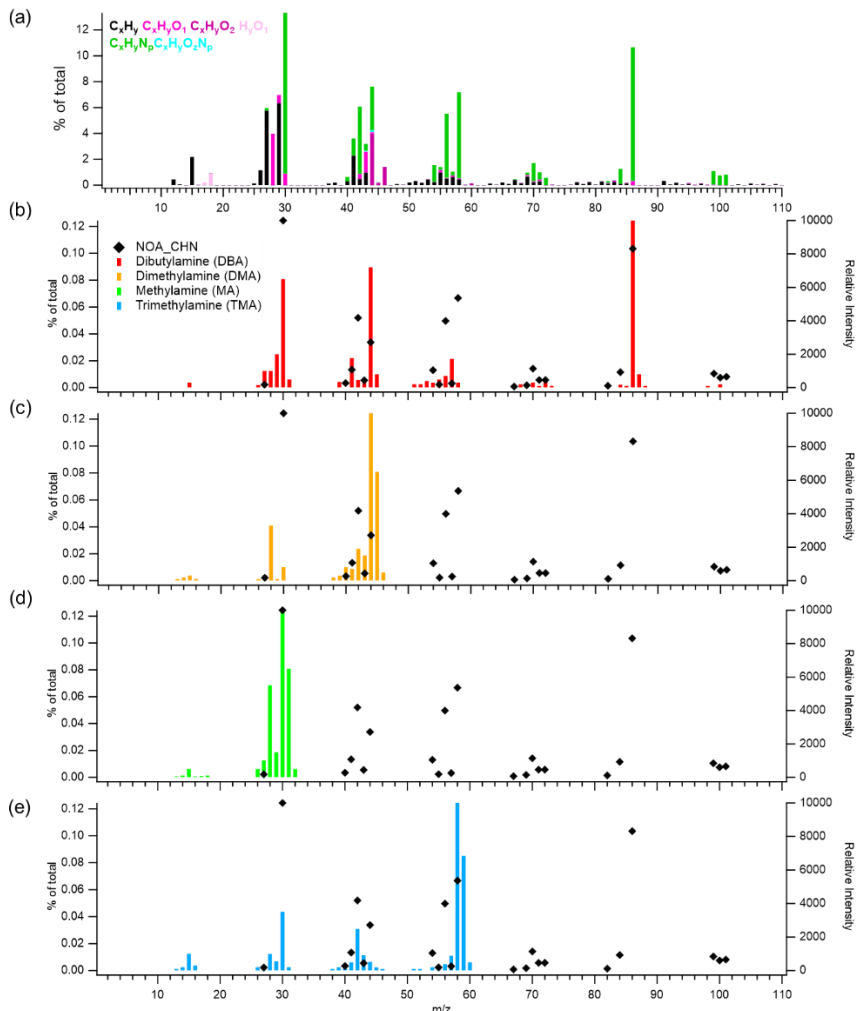
768  
769  
770  
771  
772  
773  
774  
775  
776  
777  
778

779



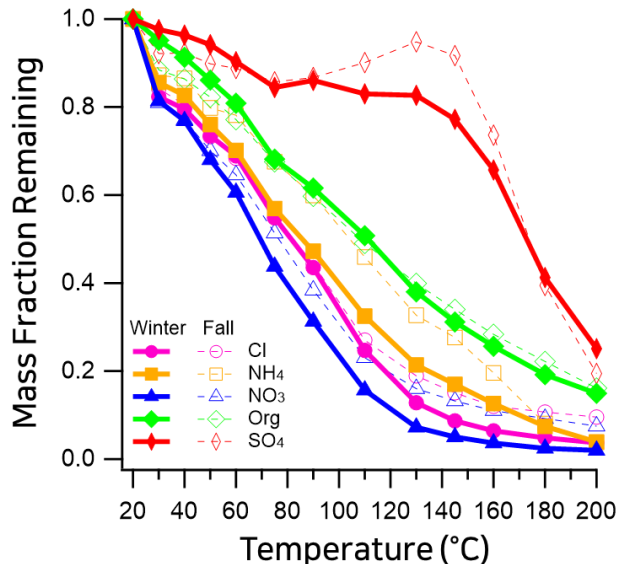
780

781 **Figure 2.** (a) Diurnal mean profiles of NOA and BBOA. Whiskers denote the 90th and 10th percentiles; box  
782 edges represent the 75th and 25th percentiles; the horizontal line indicates the median, and the colored marker  
783 shows the mean. The diurnal correlation between NOA and BBOA mean values is 0.63.  
784 (b) Relative humidity (RH)-binned nighttime (19:00–05:00) profile of NOA. Box and whisker definitions are the  
785 same as in panel (a). (c) Time series of NOA, BBOA, and amine-related ions ( $\text{CH}_4\text{N}^+$ ,  $\text{C}_2\text{H}_6\text{N}^+$ ,  $\text{C}_3\text{H}_8\text{N}^+$ ,  
786  $\text{C}_5\text{H}_{12}\text{N}^+$ ), along with their correlations with NOA and BBOA.

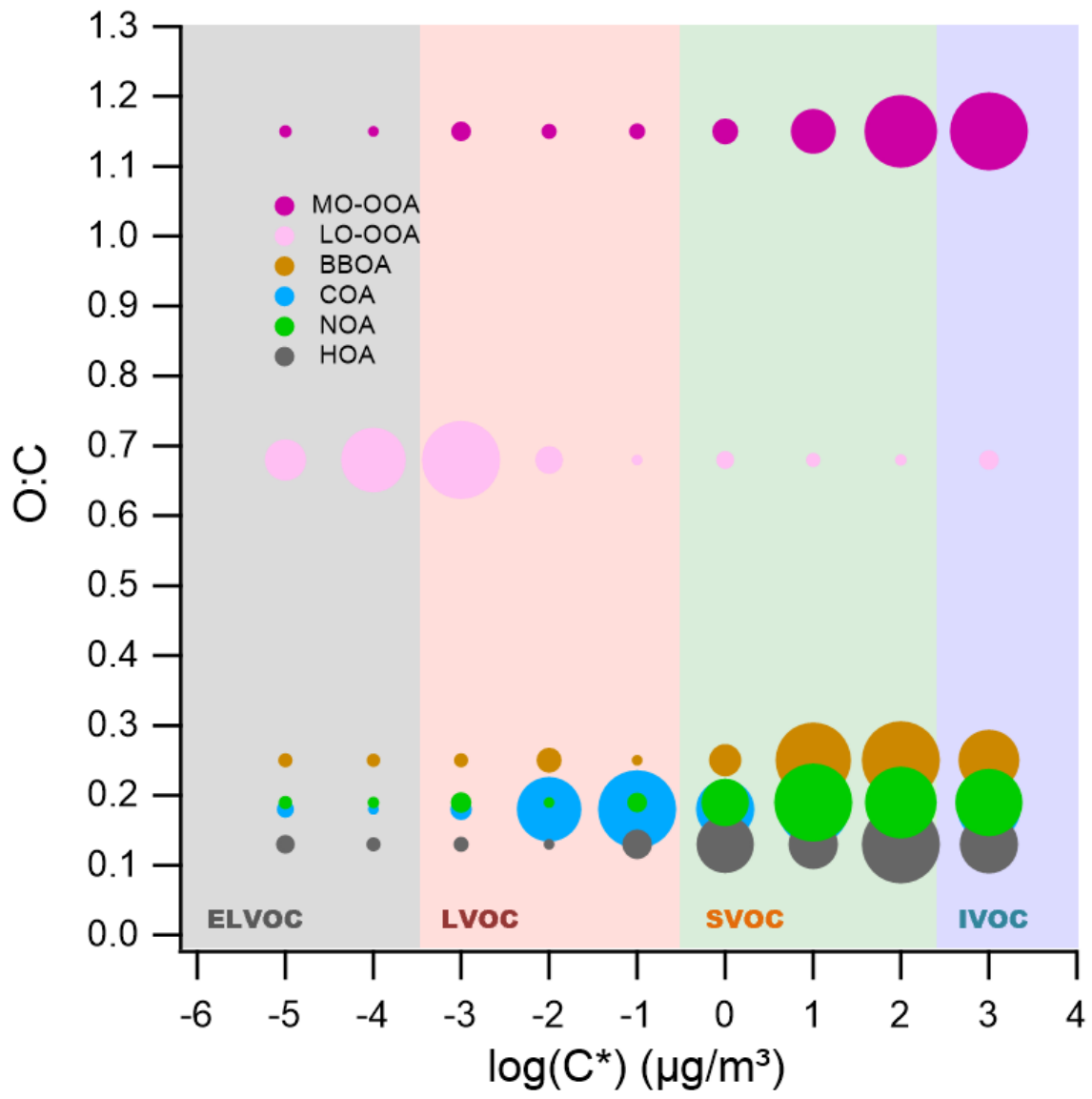


787  
 788 **Figure 3.** Mass spectra of (a) the NOA factor resolved by PMF analysis in this study, and reference spectra of amines  
 789 from the NIST library: (b) dibutylamine (DBA), (c) dimethylamine (DMA), (d) methylamine (MA), and (e)  
 790 trimethylamine (TMA). In panels (b)–(e), the left y-axis indicates the contribution of CHN-containing ions in the NOA  
 791 factor (% of total), while the right y-axis shows the relative intensity of each compound's mass spectrum from the NIST  
 792 library.

793  
 794  
 795

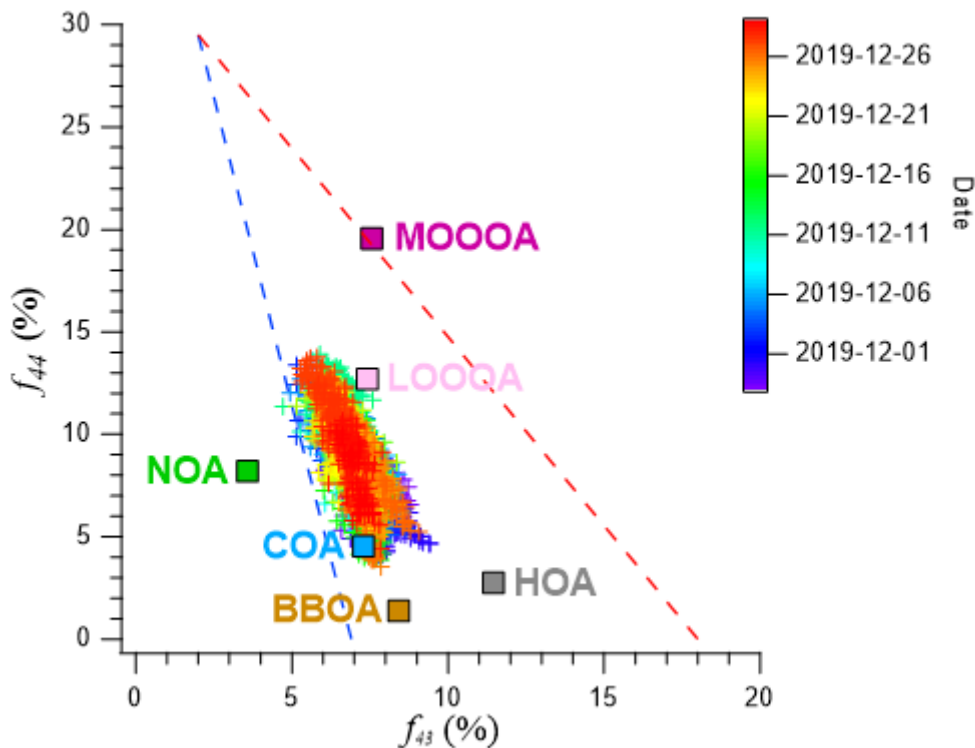


796 **Figure 4.** Mass fraction remaining (MFR) of non-refractory (NR) aerosol species measured in Seoul using a thermodenuder  
797 coupled to a high-resolution time-of-flight aerosol mass spectrometer (HR-ToF-AMS). Winter 2019 (this study; dashed) is  
798 compared with fall 2019 (previously reported; solid) (Jeon et al., 2023). Species include organics (magenta), nitrate (blue),  
799 sulfate (orange), ammonium (green), and chloride (red).

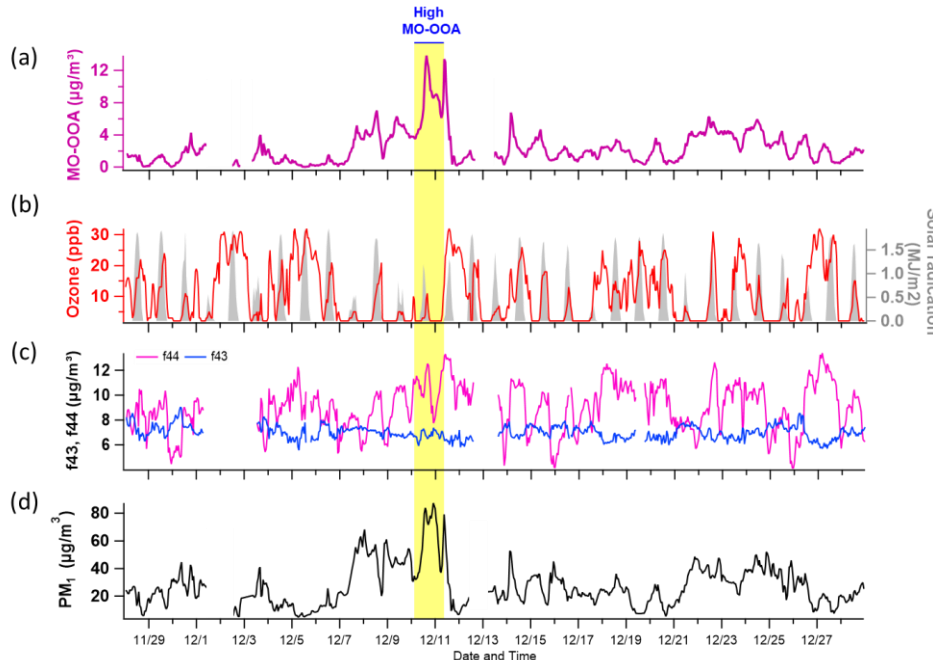


800  
 801  
 802 **Figure 5.** Two-dimensional volatility basis set (2D-VBS) representation of organic aerosol (OA) sources identified in  
 803 winter 2019 in Seoul. The plot illustrates the relationship between the oxygen-to-carbon (O:C) ratio and the effective  
 804 saturation concentration ( $C^*$ ) for each OA source resolved via positive matrix factorization (PMF). Solid circles  
 805 represent the volatility distribution across  $C^*$  bins, with marker size proportional to the mass fraction within each bin  
 806 for the given source. Shaded regions correspond to different volatility classes: extremely low-volatility organic  
 807 compounds (ELVOCs), low-volatility organic compounds (LVOCs), semi-volatile organic compounds (SVOCs), and  
 808 intermediate-volatility organic compounds (IVOCs), delineated by their  $C^*$  values.

809  
810  
811



812  
813 **Figure 6.** scatterplot of  $f_{44}$  (CO<sub>2</sub><sup>+</sup>) versus  $f_{43}$  (C<sub>2</sub>H<sub>3</sub>O<sup>+</sup>). for the measured organic aerosol. The data points are color-coded  
814 by date to illustrate the temporal variation in OA composition throughout the observation period. The separated OA factors  
815 (HOA, COA, BBOA, NOA, LO-OOA, and MO-OOA) are also shown to enable comparison of source contributions and  
816 oxidation characteristics. The dashed line represents the typical  $f_{60}$  threshold associated with biomass-burning influence,  
817 while the triangular boundary indicates the conventional oxidative aging trend in the  $f_{44}$ - $f_{60}$  space.  
818  
819  
820  
821  
822  
823



824  
825 **Figure 67.** Time series plots of (a) MO-OOA concentration, (b) ozone ( $\text{O}_3$ ) and solar radiation,  
826 (c)  $f_{44}$  and  $f_{43}$  (indicative of  
827 oxidation state), and (d) total  $\text{PM}_1$  concentration. The period characterized by elevated MO-OOA levels is highlighted in bright  
828 yellow. Panels (e)–(f) present comparative distributions of these variables—MO-OOA,  $\text{O}_3$  and solar radiation,  $f_{44}$  and  $f_{43}$ , and  
829  $\text{PM}_1$ —between the high MO-OOA period (shaded in blue) and the entire measurement period (indicated by gray hatching).

830 **References**

831 Ghim, Y. S., Moon, K.-C., Lee, S., Kim, Y. P., 2005. Visibility trends in Korea during the past two decades. *J. Air*  
832 *Waste Manag. Assoc.* 55, 73–82. <https://doi.org/10.1080/10473289.2005.10464599>

833 Zhao, H., Che, H., Zhang, X., Ma, Y., Wang, Y., Wang, H., Wang, Y., 2013. Characteristics of visibility and  
834 particulate matter (PM) in an urban area of Northeast China. *Atmos. Pollut. Res.* 4, 427–434.  
835 <https://doi.org/10.5094/APR.2013.049>

836 Hamanaka, R. B., Mutlu, G. M., 2018. Particulate matter air pollution: Effects on the cardiovascular system. *Front.*  
837 *Endocrinol.* 9, 680. <https://doi.org/10.3389/fendo.2018.00680>

838 Manisalidis, I., Stavropoulou, E., Starvropoulos, A., Bezirtzoglou, E., 2020. Environmental and health impacts of  
839 air pollution: a review. *Front. Public Health* 8, 14. <https://doi.org/10.3389/fpubh.2020.00014>

840 IPCC, 2021. Climate Change 2021: The Physical Science Basis. Contribution of Working Group I to the Sixth  
841 Assessment Report of the Intergovernmental Panel on Climate Change, edited by Masson-Delmotte, V., Zhai,  
842 P., Pirani, A., Connors, S.L., Péan, C., Berger, S., et al. Cambridge University Press, Cambridge, UK and New  
843 York, NY, USA, pp. 817–922. <https://doi.org/10.1017/9781009157896.008>

844 Zhang, Q., Jimenez, J. L., Canagaratna, M. R., Allan, J. D., Coe, H., Ulbrich, I., Alfarra, M. R., Takami, A.,  
845 Middlebrook, A. M., Sun, Y. L., Dzepina, K., Dunlea, E., Docherty, K., DeCarlo, P., Salcedo, D., Onasch, T.  
846 B., Jayne, J. T., Miyoshi, T., Shimono, A., Hatakeyama, N., Takegawa, N., Kondo, Y., Schneider, J., Drewnick,  
847 F., Weimer, S., Demerjian, K. L., Williams, P. I., Bower, K. N., Bahreini, R., Cottrell, L., Griffin, R. J.,  
848 Rautianen, J., Worsnop, D. R., 2007. Ubiquity and dominance of oxygenated species in organic aerosols in  
849 anthropogenically-influenced Northern Hemisphere mid-latitudes. *Geophys. Res. Lett.* 34, L13801.  
850 <https://doi.org/10.1029/2007GL029979>

851 Jimenez, J. L., Canagaratna, M. R., Donahue, N. M., Prevot, A. S. H., Zhang, Q., Kroll, J. H., ... Worsnop, D. R.,  
852 2009. Evolution of organic aerosols in the atmosphere. *Science* 326, 1525–1529.  
853 <https://doi.org/10.1126/science.1180353>

854 Hallquist, M., Wenger, J. C., Baltensperger, U., Rudich, Y., Simpson, D., Claeys, M., ... Seinfeld, J. H., 2009. The  
855 formation, properties and impact of secondary organic aerosol: current and emerging issues. *Atmos. Chem.*  
856 *Phys.* 9, 5155–5236. <https://doi.org/10.5194/acp-9-5155-2009>

857 Robinson, A. L., Donahue, N. M., Shrivastava, M. K., Weitkamp, E. A., Sage, A. M., Grieshop, A. P., Lane, T. E.,  
858 Pierce, J. R., Pandis, S. N., 2007. Rethinking organic aerosols: Semivolatile emissions and photochemical aging.  
859 *Science* 315, 1259–1262. <https://doi.org/10.1126/science.1133061>

860 Donahue, N. M., Robinson, A. L., Stanier, C. O., Pandis, S. N., 2006. Coupled partitioning, dilution, and chemical  
861 aging of semivolatile organics. *Environ. Sci. Technol.* 40, 2635–2643. <https://doi.org/10.1021/es052297c>

862 Ng, N. L., Canagaratna, M. R., Zhang, Q., Jimenez, J. L., Tian, J., Ulbrich, I. M., Kroll, J. H., Docherty, K. S.,  
863 Chhabra, P. S., Bahreini, R., Murphy, S. M., Seinfeld, J. H., Hildebrandt, L., Donahue, N. M., DeCarlo, P. F.,  
864 Lanz, V. A., Prévôt, A. S. H., Dinar, E., Rudich, Y., Worsnop, D. R., 2010. Organic aerosol components  
865 observed in Northern Hemispheric datasets from Aerosol Mass Spectrometry. *Atmos. Chem. Phys.* 10, 4625–  
866 4641. <https://doi.org/10.5194/acp-10-4625-2010>

867 Cappa, C. D., Jimenez, J. L., 2010. Quantitative estimates of the volatility of ambient organic aerosol. *Atmos.*  
868 *Chem. Phys.* 10, 5409–5424. <https://doi.org/10.5194/acp-10-5409-2010>

869 Sinha, A., George, I., Holder, A., Preston, W., Hays, M., Grieshop, A. P., 2023. Development of volatility  
870 distributions for organic matter in biomass burning emissions. *Environ. Sci. Adv.* 3, 11–23.  
871 <https://doi.org/10.1039/D2EA00080F>

872 Glasius, M., Goldstein, A. H., 2016. Recent discoveries and future challenges in atmospheric organic chemistry.  
873 *Environ. Sci. Technol.* 50, 2754–2764. <https://doi.org/10.1021/acs.est.5b05105>

874 Matsui, H., Koike, M., Takegawa, N., Kondo, Y., Griffin, R. J., Miyazaki, Y., Yokouchi, Y., Ohara, T., 2009.  
875 Secondary organic aerosol formation in urban air: Temporal variations and possible contributions from  
876 unidentified hydrocarbons. *J. Geophys. Res. Atmos.* 114, D02209. <https://doi.org/10.1029/2008JD010164>

877 Jiang, F., Liu, Q., Huang, X., Wang, T., Zhuang, B., Xie, M., 2012. Regional modelling of secondary organic  
878 aerosol over China using WRF/Chem. *J. Aerosol Sci.* 53, 50–61. <https://doi.org/10.1016/j.jaerosci.2011.09.003>

879 Li, J., Zhang, M., Wu, F., Sun, Y., Tang, G., 2017. Assessment of the impacts of aromatic VOC emissions and  
880 yields of SOA on SOA concentrations with the air quality model RAMS-CMAQ. *Atmos. Environ.* 158, 105–  
881 115. <https://doi.org/10.1016/j.atmosenv.2017.03.035>

882 Zhao, B., Wang, S., Donahue, N. M., Jathar, S. H., Huang, X., Wu, W., ... & Hao, J. (2016). Quantifying the effect  
883 of organic aerosol aging and intermediate-volatility emissions on regional-scale aerosol pollution in China.  
884 *Scientific Reports*, 6, 28815. <https://doi.org/10.1038/srep28815>

885 Kang, H. G., Kim, Y., Collier, S., Zhang, Q., Kim, H., 2022. Volatility of springtime ambient organic aerosol  
886 derived with thermodenuder aerosol mass spectrometry in Seoul, Korea. *Environ. Pollut.* 310, 119203.  
887 <https://doi.org/10.1016/j.envpol.2022.119203>

888 Huang, X.-F., He, L.-Y., Hu, M., Canagaratna, M. R., Sun, Y., Zhang, Q., Worsnop, D. R., 2010. Highly time-  
889 resolved chemical characterization of atmospheric submicron particles during 2008 Beijing Olympic Games

890 using an Aerodyne High-Resolution Aerosol Mass Spectrometer. *Atmos. Chem. Phys.* 10, 8933–8945.  
891 <https://doi.org/10.5194/acp-10-8933-2010>

892 Mohr, C., DeCarlo, P. F., Heringa, M. F., Chirico, R., Slowik, J. G., Richter, R., Reche, C., Alastuey, A., Querol,  
893 X., Seco, R., Peñuelas, J., Jiménez, J. L., Crippa, M., Zimmermann, R., Baltensperger, U., Prévôt, A. S. H.,  
894 2012. Identification and quantification of organic aerosol from cooking and other sources in Barcelona using  
895 aerosol mass spectrometer data. *Atmos. Chem. Phys.* 12, 1649–1665. <https://doi.org/10.5194/acp-12-1649-2012>

896

897 Xu, L., Kollman, M. S., Song, C., Shilling, J. E., Ng, N. L., 2014. Effects of NO<sub>x</sub> on the volatility of secondary  
898 organic aerosol from isoprene photooxidation. *Environ. Sci. Technol.* 48, 2253–2262.  
899 <https://doi.org/10.1021/es404842g>

900 Grieshop, A. P., Logue, J. M., Donahue, N. M., Robinson, A. L., 2009. Laboratory investigation of photochemical  
901 oxidation of organic aerosol from wood fires 1: Measurement and simulation of organic aerosol evolution.  
902 *Atmos. Chem. Phys.* 9, 1263–1277. <https://doi.org/10.5194/acp-9-1263-2009>

903 Kim, H., Zhang, Q., Bae, G.-N., Kim, J.Y., Lee, S.B., 2017. Sources and atmospheric processing of winter aerosols  
904 in Seoul, Korea: Insights from real-time measurements using a high-resolution aerosol mass spectrometer.  
905 *Atmos. Chem. Phys.* 17, 2009–2033. <https://doi.org/10.5194/acp-17-2009-2017>

906 DeCarlo, P. F., Kimmel, J. R., Trimborn, A., Northway, M. J., Jayne, A. E., Aiken, A. C., ... & Jimenez, J. L.  
907 (2006). Field-deployable, high-resolution, time-of-flight aerosol mass spectrometer. *Analytical Chemistry*,  
908 78(24), 8281–8289. <https://doi.org/10.1021/ac061249>

909 Canagaratna, M. R., Jimenez, J. L., Kroll, J. H., Chen, Q., Kessler, S. H., Massoli, P., ... & Worsnop, D. R. (2015).  
910 Elemental ratio measurements of organic compounds using aerosol mass spectrometry: Improved sensitivity  
911 and intercomparability. *Atmospheric Chemistry and Physics*, 15(1), 253–272. <https://doi.org/10.5194/acp-15-253-2015>

912

913 Paatero, P., Tapper, U., 1994. Positive matrix factorization – A nonnegative factor model with optimal utilization  
914 of error estimates of data values. *Environmetrics* 5, 111–126. <https://doi.org/10.1002/env.3170050203>

915 Ulbrich, I. M., Canagaratna, M. R., Zhang, Q., Worsnop, D. R., Jimenez, J. L., 2009. Interpretation of organic  
916 components from Positive Matrix Factorization of aerosol mass spectrometric data. *Atmos. Chem. Phys.* 9,  
917 2891–2918. <https://doi.org/10.5194/acp-9-2891-2009>

918 Zhang, Q., Jimenez, J. L., Canagaratna, M. R., Ulbrich, I. M., Ng, N. L., Worsnop, D. R., Sun, Y., 2011.  
919 Understanding atmospheric organic aerosols via factor analysis of aerosol mass spectrometry: A review. *Anal.  
920 Bioanal. Chem.* 401, 3045–3067. <https://doi.org/10.1007/s00216-011-5355-y>

921 Huffman, J. A., Docherty, K. S., Aiken, A. C., Cubison, M. J., Ulbrich, I. M., DeCarlo, P. F., Jimenez, J. L., 2009.  
922 Chemically-resolved aerosol volatility measurements from two megacity field studies. *Atmos. Chem. Phys.* 9,  
923 7161–7182. <https://doi.org/10.5194/acp-9-7161-2009>

924 Saha, P. K., Khlystov, A., Grieshop, A. P., 2014. Determining aerosol volatility parameters using a “dual  
925 thermodenuder” system: Application to laboratory-generated organic aerosols. *Aerosol Sci. Technol.* 49, 620–  
926 632. <https://doi.org/10.1080/02786826.2015.1056769>

927 Zhou, S., Collier, S., Jaffe, D. A., Briggs, N. L., Hee, J., Sedlacek III, A. J., Kleinman, L., & Lewis, K., 2017.  
928 Regional influence of wildfires on aerosol chemistry in the western US and insights into atmospheric aging of  
929 biomass burning organic aerosol. *Atmospheric Chemistry and Physics*, 17, 2477–2493.  
930 <https://doi.org/10.5194/acp-17-2477-2017>

931 Riipinen, I., Pierce, J. R., Donahue, N. M., Pandis, S. N., 2010. Equilibration time scales of organic aerosol inside  
932 thermodenuders: Kinetics versus equilibrium thermodynamics. *Atmos. Environ.* 44, 597–607.  
933 <https://doi.org/10.1016/j.atmosenv.2009.11.022>

934 Karnezi, E., Riipinen, I., Pandis, S. N., 2014. Measuring the atmospheric organic aerosol volatility distribution: a  
935 theoretical analysis. *Atmos. Meas. Tech.* 7, 2953–2965. <https://doi.org/10.5194/amt-7-2953-2014>

936 Chen, Y., Wang, Z., Wang, Y., Zheng, X., Fu, P., Kawamura, K., Zhang, Y., 2021. Characterization of nitrogen-  
937 containing organic aerosol in Guangzhou, China: seasonal variation, formation mechanism and source  
938 apportionment. *Atmos. Chem. Phys.* 21, 4329–4344. <https://doi.org/10.5194/acp-21-4329-2021>

939 Hayes, P. L., Ortega, A. M., Cubison, M. J., Froyd, K. D., Zhao, Y., Cliff, S. S., ... Jimenez, J. L., 2013. Organic  
940 aerosol composition and sources in Pasadena, California, during the 2010 CalNex campaign. *J. Geophys. Res.*  
941 *Atmos.* 118, 9233–9257. <https://doi.org/10.1002/jgrd.50530>

942 Sun, Y., Jiang, Q., Wang, Z., Fu, P., Li, J., Yang, T., Yin, Y., 2011. Investigation of the sources and evolution  
943 processes of severe haze pollution in Beijing in January 2013. *J. Geophys. Res. Atmos.* 119, 4380–4398.  
944 <https://doi.org/10.1002/2014JD021641>

945 Baek, K. M., Park, E. H., Kang, H., Ji, M. J., Park, H. M., Heo, J & Kim, H., 2022. Seasonal characteristics of  
946 atmospheric water-soluble organic nitrogen in PM2.5 in Seoul, Korea: Source and atmospheric processes of  
947 free amino acids and aliphatic amines. *Science of the Total Environment*, 807, 150785.  
948 <https://doi.org/10.1016/j.scitotenv.2021.152335>

949 Rovelli, G., Miles, R. E. H., Reid, J. P., and Clegg, S. L.: Hygroscopic properties of aminium sulfate aerosols,  
950 *Atmos. Chem. Phys.*, 17, 4369–4385, <https://doi.org/10.5194/acp-17-4369-2017>, 2017.

951 Ge, X., Wexler, A. S., Clegg, S. L., 2011. Atmospheric amines – Part I. A review. *Atmos. Environ.* 45, 524–546.  
952 <https://doi.org/10.1016/j.atmosenv.2010.10.012>

953 He, L.-Y., Lin, Y., Huang, X. F., Guo, W. W., Niu, J. L., Shen, Y. F., Sen, J., and Hu, M.: Characterization of high-  
954 resolution aerosol mass spectra of primary organic aerosol emissions from Chinese cooking and biomass  
955 burning, *Atmos. Chem. Phys.*, 10, 11535–11543, <https://doi.org/10.5194/acp-10-11535-2010>, 2010

956 You, Y., Renbaum-Wolff, L., Carreras-Sospedra, M., Dabdub, D., Bertram, A. K., Martin, S. T., et al., 2014.  
957 Images reveal that amines promote the heterogeneous reaction of epoxides in model organic aerosols. *J. Phys.*  
958 *Chem. Lett.* 5, 3211–3215. <https://doi.org/10.1021/jz501268k>

959 Yao, L., Wang, M. Y., Wang, X. K., Zhang, W. Q., Liu, Y., Li, L., et al., 2016. Atmospheric new particle formation  
960 from sulfuric acid and amines in a Chinese megacity. *Sci. Bull.* 61, 939–945. <https://doi.org/10.1007/s11434-016-1083-0>

961 Kim, H., Zhang, Q., Sun, Y., Bae, G. N., Lee, B. E., Park, K., ... & Kim, Y. J. 2020. Measurement report:  
962 Characterization of severe spring haze episodes and influences of long-range transport in the Seoul  
963 metropolitan area in March 2019. *Atmospheric Chemistry and Physics*, 20(18), 11527–11545.  
964 <https://doi.org/10.5194/acp-20-11527-2020>

965 Jeon, J., Chen, Y., Kim, H., 2023. Influence of meteorology on emission sources and physicochemical properties  
966 of particulate matter in Seoul, Korea during heating period. *Atmos. Environ.* 301, 119733.  
967 <https://doi.org/10.1016/j.atmosenv.2023.119733>

968 Zhang, Q., Alfarra, M. R., Worsnop, D. R., Allan, J. D., Coe, H., Canagaratna, M. R., ... & Jimenez, J. L. 2005.  
969 Deconvolution and quantification of hydrocarbon-like and oxygenated organic aerosols based on aerosol mass  
970 spectrometry. *Environmental Science & Technology*, 39(13), 4938–4952. <https://doi.org/10.1021/es0485681>

971 Simoneit, B. R. T. 2002. Biomass burning – a review of organic tracers for smoke from incomplete combustion.  
972 *Applied Geochemistry*, 17(3), 129–162. [https://doi.org/10.1016/S0883-2927\(01\)00061-0](https://doi.org/10.1016/S0883-2927(01)00061-0)

973 Cubison, M. J., Ortega, A. M., Hayes, P. L., Farmer, D. K., Day, D., Lechner, M. J., ... & Jimenez, J. L. 2011.  
974 Effects of aging on organic aerosol from open biomass burning smoke in aircraft and laboratory studies.  
975 *Atmospheric Chemistry and Physics*, 11(23), 12049–12064. <https://doi.org/10.5194/acp-11-12049-2011>

976 Xu, L., Williams, L. R., Young, D. E., Allan, J. D., Coe, H., Massoli, P., Fortner, E., Chhabra, P., Herndon, S.,  
977 Brooks, W. A., Jayne, J. T., Worsnop, D. R., Aiken, A. C., Liu, S., Gorkowski, K., Dubey, M. K., Fleming, Z.  
978 L., Visser, S., Prévôt, A. S. H., Ng, N. L., 2016. Wintertime aerosol chemical composition, volatility, and  
979 spatial variability in the Greater London Area. *Atmos. Chem. Phys.* 16, 1139–1160.  
980 <https://doi.org/10.5194/acp-16-1139-2016>

982 Feng, T., Wang, Y., Hu, W., Zhu, M., Song, W., Chen, W., ... Wang, X., 2023. Impact of aging on the sources,  
983 volatility, and viscosity of organic aerosols in Chinese outflows. *Atmos. Chem. Phys.* 23, 611–636.  
984 <https://doi.org/10.5194/acp-23-611-2023>

985 Scott, W. D., & Cattell, F. C. R. 1979. Vapor pressure of ammonium sulfates. *Atmospheric Environment* (1967),  
986 13(6), 987–1000. [https://doi.org/10.1016/0004-6981\(79\)90174-4](https://doi.org/10.1016/0004-6981(79)90174-4)

987 Donahue, N. M., Robinson, A. L., Pandis, S. N., 2009. Atmospheric organic particulate matter: From smoke to  
988 secondary organic aerosol. *Atmos. Environ.* 43, 94–106. <https://doi.org/10.1016/j.atmosenv.2008.09.055>

989 Ehn, M., Thornton, J. A., Kleist, E., Sipilä, M., Junninen, H., Pullinen, I., ... & Kulmala, M. 2014. A large source  
990 of low-volatility secondary organic aerosol. *Nature*, 506(7489), 476–479. <https://doi.org/10.1038/nature13032>

991 Kroll, J. H., Smith, J. D., Che, D. L., Kessler, S. H., Worsnop, D. R., Wilson, K. R., 2009. Measurement of  
992 fragmentation and functionalization pathways in the heterogeneous oxidation of oxidation organic aerosol.  
993 *Environ. Sci. Technol.* 43, 7826–7833. <https://doi.org/10.1021/es901683r>

994 Xu, W., Takeuchi, M., Chen, C., Qiu, Y., Xie, C., Xu, W., Ma, N., Worsnop, D. R., Ng, N. L., and Sun, Y.:  
995 Estimation of particulate organic nitrates from thermodenuder–aerosol mass spectrometer measurements in  
996 the North China Plain, 14, 3693–3705, <https://doi.org/10.5194/amt-14-3693-2021>, 2021.

997 Cao, L.-M., Huang, X.-F., Li, Y.-Y., Hu, M., He, L.-Y., 2018. Volatility measurement of atmospheric submicron  
998 aerosols in an urban atmosphere in southern China. *Atmos. Chem. Phys.* 18, 1729–1743.  
999 <https://doi.org/10.5194/acp-18-1729-2018>

1000 Xu, W., Xie, C., Karnezi, E., Zhang, Q., Wang, J., Pandis, S.N., Ge, X., Zhang, J., An, J., Wang, Q., et al., 2019.  
1001 Summertime aerosol volatility measurements in Beijing, China. *Atmos. Chem. Phys.* 19, 10205–10216.  
1002 <https://doi.org/10.5194/acp-19-10205-2019>

1003 Allan, J. D., Alfarra, M. R., Bower, K. N., Williams, P. I., Gallagher, M. W., Jimenez, J. L., McDonald, A. G.,  
1004 Nemitz, E., Canagaratna, M. R., and Coe, H.: Quantitative sampling using an Aerodyne aerosol mass  
1005 spectrometer—2. Measurements of fine particulate chemical composition in two U.K. cities, *J. Geophys. Res.-*  
1006 *Atmos.*, 108, 4091, 2003, <https://doi.org/10.1029/2002JD002359>.

1007 Berndt, T., Richters, S., Jokinen, T., et al.: Hydroxyl radical-induced formation of highly oxidized organic  
1008 compounds, *Nat. Commun.*, 7, 13677, 2016, <https://doi.org/10.1038/ncomms13677>.

1009 Bianchi, F., Kurtén, T., Riva, M., et al.: Highly oxygenated organic molecules (HOM) from gas-phase autoxidation  
1010 involving peroxy radicals: A key contributor to atmospheric aerosol, *Chem. Rev.*, 119, 3472–3509, 2019,  
1011 <https://doi.org/10.1021/acs.chemrev.8b00395>.

1012 Brown, S. S. and Stutz, J.: Nighttime radical observations and chemistry, *Chem. Soc. Rev.*, 41, 6405–6447, 2012,  
1013 <https://doi.org/10.1039/C2CS35181A>.

1014 Canagaratna, M. R., Jayne, J. T., Jimenez, J. L., et al.: Chemical and microphysical characterization of ambient  
1015 aerosols with the Aerodyne aerosol mass spectrometer, *Mass Spectrom. Rev.*, 26, 185–222, 2007,  
1016 <https://doi.org/10.1002/mas.20115>.

1017 Chhabra, P. S., Ng, N. L., Canagaratna, M. R., et al.: Elemental composition and oxidation of chamber organic  
1018 aerosol, *Atmos. Chem. Phys.*, 11, 8827–8841, 2011, <https://doi.org/10.5194/acp-11-8827-2011>.

1019 D'Ambro, E. L., Schobesberger, S., Gaston, C. J., et al.: Molecular composition and volatility of isoprene  
1020 photochemical oxidation secondary organic aerosol under low- and high-NO<sub>x</sub> conditions, *Atmos. Chem. Phys.*,  
1021 17, 159–174, 2017, <https://doi.org/10.5194/acp-17-159-2017>.

1022 Donahue, N. M., Epstein, S. A., Pandis, S. N., and Robinson, A. L.: A two-dimensional volatility basis set – Part  
1023 1: Organic-aerosol mixing thermodynamics, *Atmos. Chem. Phys.*, 11, 3303–3318, 2011,  
1024 <https://doi.org/10.5194/acp-11-3303-2011>.

1025 Faulhaber, A. E., Thomas, B. M., Jimenez, J. L., et al.: Characterization of a thermodenuder–particle beam mass  
1026 spectrometer system for the study of organic aerosol volatility and composition, *Atmos. Meas. Tech.*, 2, 15–  
1027 31, 2009, <https://doi.org/10.5194/amt-2-15-2009>.

1028 Ge, X., Wexler, A. S., and Clegg, S. L.: Atmospheric amines – Part III: Photochemistry and toxicity, *Atmos.*  
1029 *Environ.*, 45, 561–591, 2011, <https://doi.org/10.1016/j.atmosenv.2010.11.050>.

1030 Gil, J., Lee, Y., and Kim, Y. P.: Characteristics of HONO and its impact on O<sub>3</sub> formation in the Seoul Metropolitan  
1031 Area during KORUS-AQ, *Atmos. Environ.*, 246, 118032, 2021,  
1032 <https://doi.org/10.1016/j.atmosenv.2020.118032>.

1033 Han, K.-M., Kim, D.-G., Kim, J., et al.: Crop residue burning emissions and impact on particulate matter over  
1034 South Korea, *Atmosphere*, 13, 559, 2022, <https://doi.org/10.3390/atmos13040559>.

1035 Hanson, D. R., McMurry, P. H., Jiang, J., et al.: Ambient pressure proton transfer mass spectrometry: detection of  
1036 amines and ammonia, *Environ. Sci. Technol.*, 45, 8881–8888, 2011, <https://doi.org/10.1021/es2018817>.

1037 Hennigan, C. J., Sullivan, A. P., Collett, J. L., Jr., and Robinson, A. L.: Levoglucosan stability in biomass burning  
1038 particles exposed to hydroxyl radicals, *Geophys. Res. Lett.*, 37, L09806, 2010,  
1039 <https://doi.org/10.1029/2010GL043088>.

1040 Huffman, J. A., Ziemann, P. J., Jayne, J. T., et al.: Development and characterization of a fast-stepping  
1041 thermodenuder for chemically resolved aerosol volatility measurements, *Aerosol Sci. Technol.*, 42, 395–407,  
1042 2008, <https://doi.org/10.1080/02786820802104981>.

1043 Kim, K., Park, R., Lee, Y., et al.: An investigation into atmospheric nitrous acid (HONO) and its sources in East  
1044 Asia, *Atmos. Chem. Phys.*, 24, 12575–12593, 2024, <https://doi.org/10.5194/acp-24-12575-2024>.

1045 Kroll, J. H. and Seinfeld, J. H.: Chemistry of secondary organic aerosol: Formation and evolution of low-volatility  
1046 organics in the atmosphere, *Atmos. Environ.*, 42, 3593–3624, 2008,  
1047 <https://doi.org/10.1016/j.atmosenv.2008.01.003>.

1048 Kroll, J., Donahue, N., Jimenez, J., et al.: Carbon oxidation state as a metric for describing the chemistry of  
1049 atmospheric organic aerosol, *Nat. Chem.*, 3, 133–139, 2011, <https://doi.org/10.1038/nchem.948>.

1050 Kwon, S., Won, S. R., Lim, H. B., et al.: Relationship between PM1.0 and PM2.5 in urban and background areas  
1051 of the Republic of Korea, *Atmos. Pollut. Res.*, 14, 101858, 2023, <https://doi.org/10.1016/j.apr.2023.101858>.

1052 Lamb, K. D., Kim, B.-G., and Kim, S.-W.: Estimating source-region influences on black carbon in South Korea  
1053 using the BC/CO ratio, *J. Geophys. Res.-Atmos.*, 123, 11, 2018, <https://doi.org/10.1029/2018JD029257>.

1054 Lambe, A. T., Onasch, T. B., Massoli, P., et al.: Transitions from Functionalization to Fragmentation Reactions of  
1055 Laboratory Secondary Organic Aerosol (SOA) Generated from the OH Oxidation of Alkane Precursors,  
1056 *Environ. Sci. Technol.*, 46, 5430–5437, 2012, <https://doi.org/10.1021/es300274t>.

1057 López-Hilfiker, F. D., Mohr, C., Ehn, M., et al.: A novel method for online analysis of gas and particle composition:  
1058 description and evaluation of a Filter Inlet for Gases and AEROSols (FIGAERO), *Atmos. Meas. Tech.*, 7, 983–  
1059 1001, 2014, <https://doi.org/10.5194/amt-7-983-2014>.

1060 López-Hilfiker, F. D., Mohr, C., Ehn, M., et al.: Molecular composition and volatility of organic aerosol in the  
1061 Southeastern U.S. using FIGAERO–CIMS with comparison to AMS, *Environ. Sci. Technol.*, 50, 2200–2209,  
1062 2016, <https://doi.org/10.1021/acs.est.5b04769>.

1063 Mao, J., Wang, L., Lu, C., et al.: High-resolution modeling of gaseous methylamines over a polluted region in  
1064 China: source-dependent emissions and implications of spatial variations, *Atmos. Chem. Phys.*, 18, 7933–7950,  
1065 2018, <https://doi.org/10.5194/acp-18-7933-2018>.

1066 Matsui, H., Koike, M., Kondo, Y., et al.: An estimation of the organic aerosol component in PM2.5 using AMS  
1067 and CMB models, *J. Geophys. Res.-Atmos.*, 114, D21203, 2009, <https://doi.org/10.1029/2009JD012170>.

1068 Nault, B. A., Campuzano-Jost, P., Day, D. A., et al.: Secondary organic aerosol production from local emissions  
1069 dominates over Seoul during KORUS-AQ, *Atmos. Chem. Phys.*, 18, 17769–17800, 2018,  
1070 <https://doi.org/10.5194/acp-18-17769-2018>.

1071 Nielsen, C. J., Herrmann, H., and Weller, C.: Atmospheric chemistry and environmental impact of the use of amines  
1072 in carbon capture and storage (CCS), *Chem. Soc. Rev.*, 41, 6684–6704, 2012,  
1073 <https://doi.org/10.1039/C2CS35059A>.

1074 Slater, E. J., Gkatzoflias, D., Wang, Y., et al.: Elevated levels of OH observed in haze events during wintertime  
1075 Beijing, *Atmos. Chem. Phys.*, 20, 14847–14871, 2020, <https://doi.org/10.5194/acp-20-14847-2020>.

1076 Sun, Y., Zhang, Q., Schwab, J. J., et al.: Characterization of the sources and properties of organic aerosol from  
1077 AMS measurements during a winter campaign in Beijing, China, *Atmos. Chem. Phys.*, 10, 8951–8971, 2010,  
1078 <https://doi.org/10.5194/acp-10-8951-2010>.

1079 Tiszenkel, L., Flynn, J. H., and Lee, S.-H.: Measurement report: Urban ammonia and amines in Houston, Texas,  
1080 *Atmos. Chem. Phys.*, 24, 11351–11363, 2024, <https://doi.org/10.5194/acp-24-11351-2024>.

1081 Yoo, H., Lee, H., and Kim, Y. P.: Insights from single-particle analysis: submicron aerosol composition in Seoul  
1082 during KORUS-AQ, *Atmos. Chem. Phys.*, 24, 853–872, 2024, <https://doi.org/10.5194/acp-24-853-2024>.

1083 Ziemann, P. J. and Atkinson, R.: Kinetics, products, and mechanisms of secondary organic aerosol formation from  
1084 gas-phase reactions of organic compounds, *Chem. Soc. Rev.*, 41, 6582–6605, 2012,  
1085 <https://doi.org/10.1039/C2CS35122F>.

1086 Paciga, A., Young, D. E., Ward, M. W., et al.: Volatility of organic aerosol and its components in the megacity of  
1087 Paris, *Atmos. Chem. Phys.*, 16, 2013–2031, 2016, <https://doi.org/10.5194/acp-16-2013-2016>.

1088 Ge, X., Wexler, A. S., and Clegg, S. L.: Atmospheric amines – Part II. Thermodynamic properties and gas-particle  
1089 partitioning, *Atmos. Chem. Phys.*, 11, 55–69, 2011, <https://doi.org/10.5194/acp-11-55-2011>.

1090 Xu, W., Sun, Y., Wang, Q., et al.: Seasonal characterization of organic nitrogen in atmospheric aerosols using high-  
1091 resolution aerosol mass spectrometry in Beijing, China, *ACS Earth Space Chem.*, 1, 649–658, 2017,  
1092 <https://doi.org/10.1021/acsearthspacechem.7b00106>.

1093 Sun, Y. L., Zhang, Q., Schwab, J. J., et al.: Characterization of the sources and processes of organic and inorganic  
1094 aerosols in New York City with a high-resolution time-of-flight aerosol mass spectrometer, *Atmos. Chem.*  
1095 *Phys.*, 11, 1581–1602, 2011, <https://doi.org/10.5194/acp-11-1581-2011>.

1096 Saarikoski, S., Carbone, S., Decesari, S., et al.: Chemical characterization of springtime submicrometer aerosol in  
1097 Po Valley, Italy, *Atmos. Chem. Phys.*, 12, 8401–8421, 2012, <https://doi.org/10.5194/acp-12-8401-2012>.

1098 Silva, P. J., Erupe, M. E., Price, D., et al.: Trimethylamine as precursor to secondary organic aerosol formation via  
1099 nitrate radical reaction in the atmosphere, *Environ. Sci. Technol.*, 42, 4689–4696, 2008,  
1100 <https://doi.org/10.1021/es703016v>

1101 EPA: EPA Positive Matrix Factorization (PMF) 5.0 Fundamentals and User Guide, U.S. Environmental Protection  
1102 Agency, 2014. [https://www.epa.gov/sites/default/files/2015-02/documents/pmf\\_5.0\\_user\\_guide.pdf](https://www.epa.gov/sites/default/files/2015-02/documents/pmf_5.0_user_guide.pdf)

1103 Waked, A., Favez, O., Alleman, L.Y., Piot, C., Petit, J.E., Delaunay, T., Verlinden, E., Jayne, J., Sciare, J., 2014.  
1104 Source apportionment of PM10 in a north-western Europe regional urban background site (Lens, France) using

1105 positive matrix factorization and including primary emissions. *Atmos. Chem. Phys.* 14, 3325–3346.  
1106 <https://doi.org/10.5194/acp-14-3325-2014>

1107 Soleimani, M., Ebrahimi, Z., Mirghaffari, N., Naseri, M., 2022. Source identification of polycyclic aromatic  
1108 hydrocarbons associated with fine particulate matters (PM<sub>2.5</sub>) in Isfahan City, Iran, using diagnostic ratio and  
1109 PMF model. *Environ. Sci. Pollut. Res.* 29, 30310–30326. <https://doi.org/10.1007/s11356-021-17635-8>

1110 Allan, J. D., Williams, P. I., Morgan, W. T., et al.: Contributions from transport, solid fuel burning and cooking to  
1111 primary organic aerosols in two UK cities, *Atmos. Chem. Phys.*, 10, 647–668, 2010,  
1112 <https://doi.org/10.5194/acp-10-647-2010>.

1113 Mohr, C., DeCarlo, P. F., Heringa, M. F., et al.: Identification and quantification of organic aerosol from cooking  
1114 and other sources in Barcelona using aerosol mass spectrometer data, *Atmos. Chem. Phys.*, 12, 1649–1665,  
1115 2012, <https://doi.org/10.5194/acp-12-1649-2012>.

1116 Sun, Y.-L., Zhang, Q., Schwab, J. J., et al.: Characterization of the sources and processes of organic aerosols in  
1117 New York City with a high-resolution time-of-flight aerosol mass spectrometer, *Atmos. Chem. Phys.*, 11,  
1118 1581–1602, 2011, <https://doi.org/10.5194/acp-11-1581-2011>.

1119